https://doi.org/10.1016/j.trgeo.2021.100574

Influences of buried depth and grain size distribution on seepage erosion in granular soils around tunnel by coupled CFD-DEM approach

Author 1

Jian-Gu QIAN, Professor

College of Architecture and Civil Engineering, Xinjiang University, Urumqi 830047, China; Key Laboratory of Geotechnical and Underground Engineering of Ministry of Education, China; Department of Geotechnical Engineering, College of Civil Engineering, Tongji University, China.

Author 2

Wei-Yi LI, PhD candidate

Key Laboratory of Geotechnical and Underground Engineering of Ministry of Education, China; Department of Geotechnical Engineering, College of Civil Engineering, Tongji University, China.

Author 3

Zhen-Yu YIN, Associate Professor

Department of Civil and Environmental Engineering, The Hong Kong Polytechnic University, Hung Hom, Kowloon, Hong Kong, China.

Author 4

Yi YANG, Assistant Professor

Department of Civil Engineering, Chu Hai College of Higher Education, Hong Kong, P.R. China.

*Corresponding author

Zhen-Yu YIN, Tel: +852 3400 8470; Fax: +852 2334 6389;
Email: zhenyu.yin@polyu.edu.hk, zhenyu.yin@gmail.com

Abstract:

For tunnels built in the saturated silty sand ground, fine particles may be migrated into tunnels through seams of tunnel segmental joints and then seepage erosion is triggered, which may induce ground settlement. However, the process from fine particles erosion to the stress redistribution and soil properties' change surrounding the tunnel and ground settlement has not been clarified up to now. For this purpose, five numerical tests of seepage erosion in granular soils around the tunnel are conducted using the Computational Fluid Dynamics and Discrete Element Method (CFD-DEM) coupling method. The influences of buried depth and grain size distribution (GSD) of gap graded soils (mainly controlled by the fines content and mean particle size ratio from coarse to fine) on the seepage erosion around the tunnel are investigated. Eroded mass, fines loss mode, surface vertical displacement, stress redistribution, fabric anisotropy, soil behavior and water pressure around the tunnel during the seepage erosion process for five tests are presented and compared. The following results can be upscaled to the practical tunnel engineering, such as: (1) the number of fines loss, the eroded zone and the ground settlement increase with buried depth and mean particle size ratio; (2) the earth pressure near the crack significantly increases due to the stress redistribution induced by fines loss, and the stress redistributed area expands with buried depth; (3) the strength and stiffness of granular soils around the crack are significantly reduced by the seepage erosion. All results revealed that the CFD-DEM simulations provide a new sight on understanding the mechanics of tunnel seepage erosion from a microscopic perspective.

Keywords: CFD-DEM; seepage; suffusion; tunnel; grading; silty sand

1. Introduction

Regarding tunnels assembled with segmental lining, segmental joints may open and dislocate due to the tunnel convergence and differential longitudinal settlement (Shen et al., 2014; Wu et al., 2015, 2014). Then, tunnel leakage occurs through the opened and dislocated segmental joints (Lyu et al., 2019; X.-W. Wang et al., 2019; Z.-F. Wang et al., 2019; Xu et al., 2019). When tunnels are built in saturated sand or silty sand, which is highly permeable soil, neither the reduction in the pore pressure nor ground and tunnel settlement will be caused by the tunnel leakage (Zhang et al., 2015, 2012). Nevertheless, for the low cohesive force between the silt/sand particles, fine particles can be easily eroded by the drag force induced by the tunnel leakage through the broken segmental joints. This erosion of fine particles then causes the ground loss with increasing the void ratio of soils. The increase of the void ratio could result in a severe reduction in the strength and stiffness of the soils around the tunnel (Chang and Yin, 2011; Yang et al., 2019a; Yin et al., 2016b, 2014). Then under the combination of the strength reduction and external loads, a further settlement will be induced up to severe engineering hazards. However, up to now, the seepage erosion induced hazards have been mainly focused on earth dams/dikes (Chang and Yin, 2011; Fox et al., 2006; Midgley et al., 2012; Richards and Reddy, 2007; Wan and Fell, 2004; Yang et al., 2019b, 2017; Yin et al., 2016a), little attention was paid to the tunnel engineering.

Previous researches on piping and suffusion in earth dams can provide valuable insight for studying seepage erosion around the tunnel, although they are two different problems. According to relative research about earth dams, the erosion process is affected by factors like the grain size distribution (GSD), the confining pressure, hydraulic pressure, and the controlling constriction size. For instance, Kenney and Lau (1985) put forward an H-F geometrical curve to differentiate between the stable grading and the unstable grading for fine particle erosion. Tomlinson and Vaid (2000) stated that high confining pressure can induce the collapse of arching bridges that cross the inter-particle voids and are assembled by the fine particles. Thus, more significant particle erosion occurs. Kenney et al. (1985) defined the controlling constriction size as the diameter of the largest soil particles that can be carried through the granular soil filter by seepage. The controlling constriction size distribution is closely related to GSD, material relative density and the cumulative number of eroded particles (Indraratna et al., 2007; Reboul et al., 2010).

No matter seepage erosion around tunnel or piping and suffusion in earth dams, the interaction of soil particles and water is involved. Among many numerical methods, the CFD-DEM coupling method has been proved to be a promising method for investigating the seepage erosion, specifically the migration and erosion of fine particles (Cheng et al., 2018; Shi et al., 2018; Sibille et al., 2015; Zhao and Shan, 2013). The method can both consider the effect of fluid and provide an insight of fundamental physics. The discrete element method (DEM) proposed by Cundall and Strack (Cundall and Strack, 1979) has been recognized as an effective numerical tool to explore the macroscopic behavior of granular materials at the particulate level. Recently, some studies using DEM investigated the macro and micro responses of soil to propose micromechanical models (Jiang et al., 2020; Liu et al., 2020; Xiong et al., 2019). DEM is a powerful numerical method for calculating the motion of many particles in the simulation of particle erosion involving large deformation and discontinuous. Soil is treated as an assembly of discrete particles in DEM. The calculation of DEM starts with the basic constitutive laws at inter-particle contacts at the particulate level and develops into the responses of the particle assembly under different loading conditions on the macroscopic scale. Consequently, the large deformation and discontinuous process of granular materials under quasi-static and dynamic conditions can be simulated (Jiang et al., 2016; Jiang and Yin, 2014, 2012). While the large deformation and discontinuous process in the FEM simulation about internal erosion are difficult to be achieved or usually simplified by many assumptions. In the post-processing section, the microstructure such as force transmission and contact network of granular materials can be measured in DEM, while it is impossible to know in FEM. Therefore, the fundamental mechanism of granular materials can be better understood in DEM simulation. The coupling of CFD and DEM inherits all the advantages of DEM and can consider the action of fluid at the same time. This combination makes it possible to investigate the interaction between particles and fluid at the microscopic level.

Recently, Zhang et al. (2019) successfully conducted a series of numerical tests using the coupled CFD-DEM method to investigate the seepage erosion mechanism of soils around shield tunnels. The quantitative relationships between the loss of fines, the volumetric strain and four influencing factors (i.e. time, hydraulic pressure, consolidated stress ratio and void ratio) have been obtained. However, the study was only focused on the localized area of soils around the tunnel at the element level. Several shortcomings, such as the simulation of the complicated flow field and stress field in actual condition, still cannot be remedied.

The major objectives of this paper are as follows: (1) to investigate the seepage erosion mechanism of gap graded silty sand around tunnels under various buried depths and GSDs (mainly fines content and mean particle size ratio from coarse to fine), and (2) to obtain the influence of the seepage erosion in the soil around tunnel including the ground surface, void ratio, stress redistribution, soil fabric, soil behavior and water pressure. To achieve these objectives, five CFD-DEM numerical models of seepage erosion in granular soils around the tunnel are prepared and conducted with various buried depths and GSDs. The results are discussed in terms of the fines loss, stress distribution, mechanical properties of soil under tunnel crack and pore pressure around the tunnel.

2. Description of coupled CFD-DEM method

In this paper, the combination of the DEM and the CFD calculation is enabled by the open-source software CFDEM (http://www.cfdem.com). It is based on the OpenFOAM CFD modeling environment (http://www.openfoam.org) and the LIGGGHTS (LAMMPS improved for general granular and granular heat transfer simulations) (http://www.liggghts.com). To simulate the actual situation and output the available fluid information as much as possible, more and more four-way instead of two-way coupling methods are adopted in CFD-DEM simulation (Jing et al., 2016). Coupling both momentum and volume of solids on fluids and fluids on solids, which is often called four-way coupling, can be achieved by the CFDEM code.

A critical issue of the four-way coupling method is the precise calculation of the void fraction of grid cells, since previous researches (Kawaguchi et al., 2000; Kloss et al., 2012; Link et al.,

2005) have pointed out that inaccuracy may occur when the particle size approaches the cell size. However, if we keep the cell size larger enough than the particle size in this study, the grid will be too coarse to get the precise result, too. To overcome the dilemma, the porous sphere model according to Jing et al. (2016) was adopted in this study to ensure the accuracy of the results while using a relatively fine grid. The principle and validations of the porous sphere model can be found in (Jing et al., 2016).

In this study, the unresolved CFD-DEM approach was chosen. The governing equation (volume-averaged Navier-Stokes equations) describing the motion of an incompressible-fluid phase in the presence of a solid phase can be written as (Kloss et al., 2012):

$$(\partial \alpha_f) / \partial t + \nabla \bullet (\alpha_f u_f) = 0 \qquad (1)$$

$$\frac{\partial \alpha_f \boldsymbol{u}_f}{\partial t} + \nabla \bullet \alpha_f \boldsymbol{u}_f \boldsymbol{u}_f = -\alpha_f \nabla \frac{p}{\rho_f} - \boldsymbol{R}_{pf} + \nabla \bullet (\alpha_f \boldsymbol{\tau}) \qquad (2)$$

where α_f is the volume fraction occupied by the fluid, ρ_f and $\boldsymbol{u}_f$ are the fluid density and fluid velocity respectively, and $\boldsymbol{\tau}$ is the stress tensor of the fluid phase. $\boldsymbol{R}_{pf}$ is the momentum exchange with the solid phase. The momentum exchange for each cell is collected from the relevant particles' drag force.

To solve the above-mentioned equations, a pressure-based solver, which adopts PISO pressure velocity coupling is used. The coupling scheme of this CFD-DEM model is shown in Fig. 1(refer to (Jing et al., 2016)).

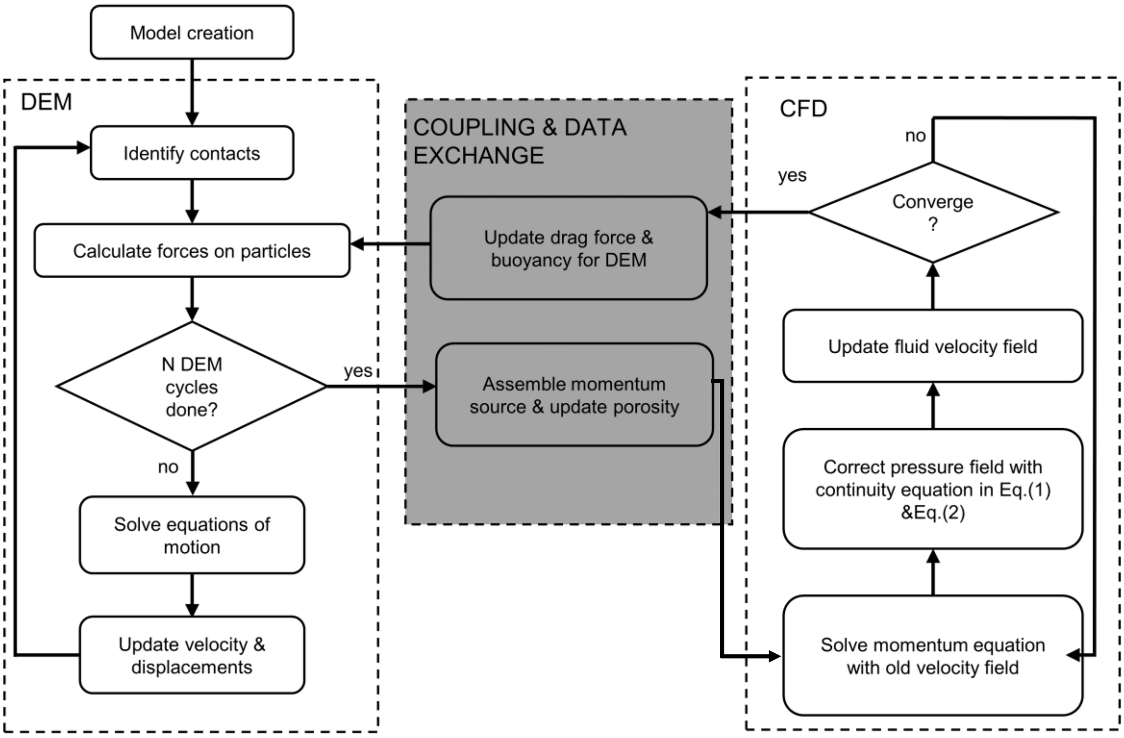

Fig. 1. Computational fluid dynamics and discrete element method (CFD-DEM) coupling scheme

The momentum exchange per unit volume applied by the particles to the fluid in each fluid element is defined as

$$\boldsymbol{R}_{pf} = \boldsymbol{K}_{pf}(\boldsymbol{u}_f - \langle \boldsymbol{u}_p \rangle) \tag{3}$$

where $\langle \boldsymbol{u}_p \rangle$ is the cell-based ensemble averaged particle velocity. To calculate $\boldsymbol{K}_{pf}$, kinds of drag correlations have been put forward in recent years (Kafui et al., 2002; Koch and Hill, 2001; Tsuji et al., 2008; Zhu et al., 2007). This paper adopted a widely used drag correlation proposed by Gidaspow et al. (1991), which is a combination of the Wen and Yu (1966) model and the Ergun equation (ERGUN and S., 1952).

When $\alpha_f > 0.8$, the momentum exchange is calculated as:

$$\boldsymbol{K}_{pf} = \frac{3}{4}\frac{(1-\alpha_f)|\boldsymbol{u}_f - \boldsymbol{u}_p|}{d_p}\alpha_f^{-2.65} \tag{4}$$

$$C_d = \frac{24}{\alpha_f Re_p}\left[1 + 0.15(\alpha_f Re_p)^{0.687}\right] \tag{5}$$

$$Re_p = \frac{|\,\boldsymbol{u}_f - \boldsymbol{u}_p|}{\upsilon_f} d_p \tag{6}$$

When $\alpha_f \leq 0.8$, the Ergun equation is applied:

$$\boldsymbol{K}_{pf} = 150\frac{(1-\alpha_f)^2 \upsilon_f}{\alpha_f {d_p}^2} + 1.75\frac{(1-\alpha_f)|\,\boldsymbol{u}_f - \boldsymbol{u}_p|}{d_p} \tag{7}$$

The DEM code of Ligghts is used to build solid phase models. The inter-particle contact and the particle-wall contact in normal and tangential directions are modeled by the simplified Hertz-Mindlin contact model. The contacts in both normal and tangential directions contain a spring with nonlinear stiffness coefficients, a dashpot and a divider which resets the contact force to zero in the condition of separated particles. Besides, a slider is set especially in the tangential direction to trigger slip once the tangential force exceeds the normal force times the friction coefficient. In Chand et al. (2012), the equations of the contact model can be found in detail.

More details about the unresolved CFD-DEM approach can also be found in the literature (Goniva et al., 2012; Kloss et al., 2012). Note that both the scaling effect and the number of particles need to be considered in DEM simulations. According to previous studies Karim (2005) and Maynar and Rodríguez (2005), the ratio of model size to the mean particle size is of more interests and is recommended to be no less than 10, which is followed in this stduty. Besides, in the open-source software OpenFOAM, the fluid condition can be rep-defined as laminar flow throughout the whole simulation. As a result, the laminar flow is ensured, and there is no effect on the particle-fluid interaction forces by changing the viscosity coefficient.

3. Simulation process

3.1 Properties and mechanical behavior of granular soil

Spherical particles are adopted in this study to reduce computational effort. There are three GSDs in the DEM part of our CFD-DEM simulations, shown in Fig. 2. According to Kenney and Lau (1985), the particles finer than d would be likely to be eroded from a soil matrix if particles of grain size from d to $4d$ occupied a less content proportion than particles of grain size less than d. Therefore, the GSD follows the gap-graded pattern proposed by Wan and Robin (Wan and Fell, 2004), which has been widely used to study the erosion related issues. The gap-graded GSD method divides the particles into two simplified categories of coarse and fine particles. The three kinds of GSD differentiate from each other by the percentage of fine particles (f_c) and the mean size ratio of coarse particles to fine particles (f_r).

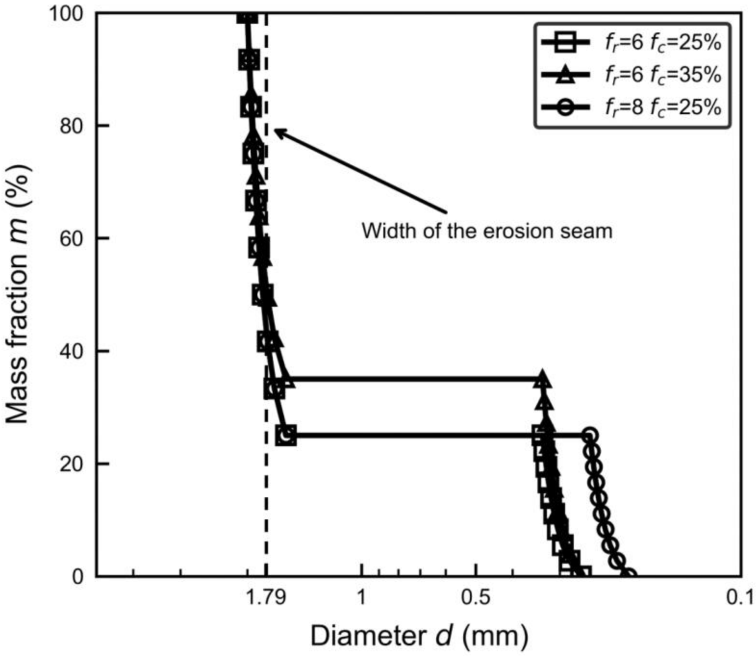

Fig. 2. Grain size distributions of gap-graded granular material in numerical simulations

Particle parameters are listed in

Table 1. A granular density of 2650 kg/m^3 and a friction coefficient of 0.3 are adopted based on previous studies (Jiang and Yin, 2014; D.-M. Zhang et al., 2019). Moreover, Young's

modulus is $2.5\times10^{8}Pa$ to ensure that the overlap in the CFD-DEM simulations is not larger than 2% of the total solid volume. The parameters of the fluid cell are derived based on the behavior of pure water under the pressure of 100 kPa and the temperature of $20^{\circ}C$.

Table 1 Parameters for DEM simulation

Parameter	**Value**
Coefficient of restitution	0.5
Poisson's ratio	0.25
Young's modulus	$2.5\text{x}10^{8}$ Pa
Coefficient of friction, particle-particle	0.3
Coefficient of friction, particle-wall	0
Particle density	2650 kg/m^3
Timestep	$1\text{x}10^{-7}$ s

The hydraulic conductivity is a predominant property of soil and is greatly affected by GSD and void ratio (Skempton and Brogan, 1994).To know the difference between the hydraulic conductivity of materials adopted in the tunnel seepage simulation, three downward seepage flow tests on three soil samples (f_r=6 and f_c=25%, f_r=6 and f_c=35%, f_r=8 and f_c=25%) were conducted. The downstream filter is composed of a 0.833 mm (2.5 times the maximum fine particle diameter) pore opening grid. Such a pore opening allows the migration of fines.GSDs are shown in Fig. 2, and the prepared void ratio is 0.35, which is close to the soil in the tunnel model (Table 2). The measurement method of hydraulic conductivity refers to the laboratory test (Rochim et al., 2017). The model dimension is 15mm, 15mm, 30mm respectively in length, wide and height. A single-staged hydraulic gradient of 4 was applied. Corresponding results are shown in Fig. 3, from which the permeability of three samples are obtained: The hydraulic conductivities of all the three samples grow first and then tend to be stable. The sample with f_r=6 and f_c=25% and the sample with f_r=6 and f_c=35% have a close hydraulic conductivity while the hydraulic conductivity of the sample with f_r=8 and f_c=25% is about half of the former two.

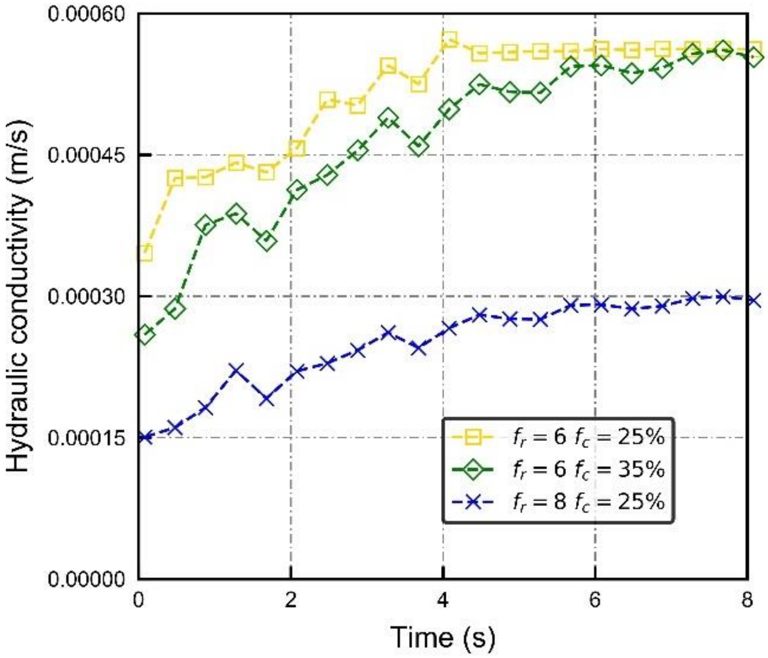

Fig. 3. Hydraulic conductivity of samples with different GSDs

Table 2 Summary information of DEM models

Model No.	C/D	Fines content, f_c	Particle diameter ratio of coarse particles to fine particles, f_r	Number of particles	Void ratio, e
Model-1	0.5	25%	6	97207	0.348
Model-2	1.0	25%	6	152319	0.343
Model-3	1.5	25%	6	204894	0.337
Model-4	0.5	35%	6	128040	0.351
Model-5	0.5	25%	8	236662	0.347

3.2 CFD-DEM models for seepage erosion around tunnel

Five numerical models of seepage erosion around the tunnel with different GSDs and different buried depths (expressed by the ratio of the depth of tunnel top to the tunnel diameter, C/D = 0.5, 1, 1.5) were prepared and conducted. All models are summarized in Table 2. Similar to previous studies (Jiang and Yin, 2012), 100g Gravity acceleration ($9.81m/s^2 \times 100$) was adopted in the numerical experiments to simulate centrifuge test conditions.

The size and shape of the DEM model are presented in detail in Fig. 4. There are three different heights (z) (28mm, 42mm, 56mm) corresponding to three different overburden-to-diameter ratios (C/D = 0.5, 1, 1.5) in these models. The width (x) and depth (y) of the model and the diameter of the tunnel (D) are 30 mm, 10 mm and 28 mm respectively.

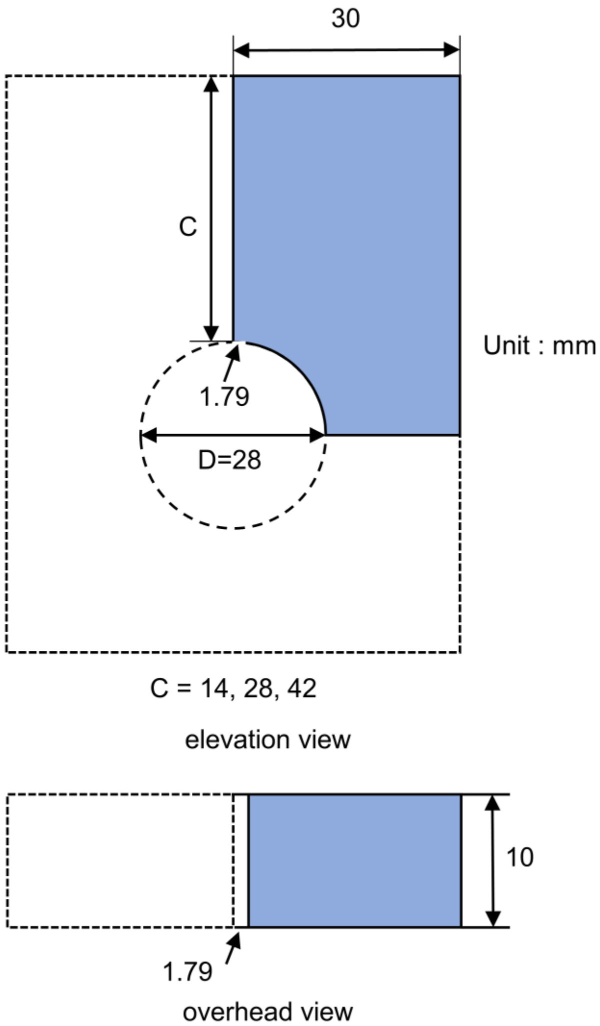

Fig. 4. Schematic diagram of seepage erosion model

Since the change induced by seepage erosion mainly occurs above the tunnel, the lower half part of the tunnel is not considered in the simulations. Also according to the symmetry, only half of the model was considered. These simplifications aim to reduce the number of particles in DEM and cells in CFD as much as possible and thus to reduce computational cost.

In the above DEM models, the tunnel is represented by the wall element in LIGGGHTS and a shorter curved wall represents the tunnel with a crack, as seen in Fig. 5. The width of this crack is set to be 1.79 mm, aiming to guarantee as many eroded fines as possible without the loss of coarse particles. For the limitation of the CFD-DEM coupling method (CFDEM), neither moving wall nor moving CFD boundary can be realized. Therefore, the tunnel is assumed to be fixed during the process of seepage erosion, and this assumption is reasonable as soil particles are the main concern.

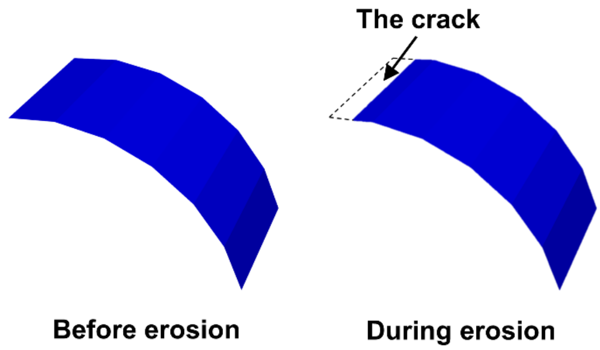

Fig. 5. Curved walls representing tunnel and tunnel with crack

In the generation of these models, the Multi-layer Method according to Jiang and Yin (Jiang and Yin, 2014, 2012; Jiang et al., 2003) was adopted to ensure the homogeneity of the ground as much as possible. The void ratio of each DEM model is summarized in Table 2. The void ratio (e) decreases slightly with the increasing buried depth for Models 1, 2 and 3 due to gravity. For Models 1, 4 and 5 to study the influence of GSD (i.e. fines content and mean particle size ratio), the void ratio of the models is roughly the same, so that the influence of the initial void ratio can be ignored. All generated DEM models are presented in Fig. 6.

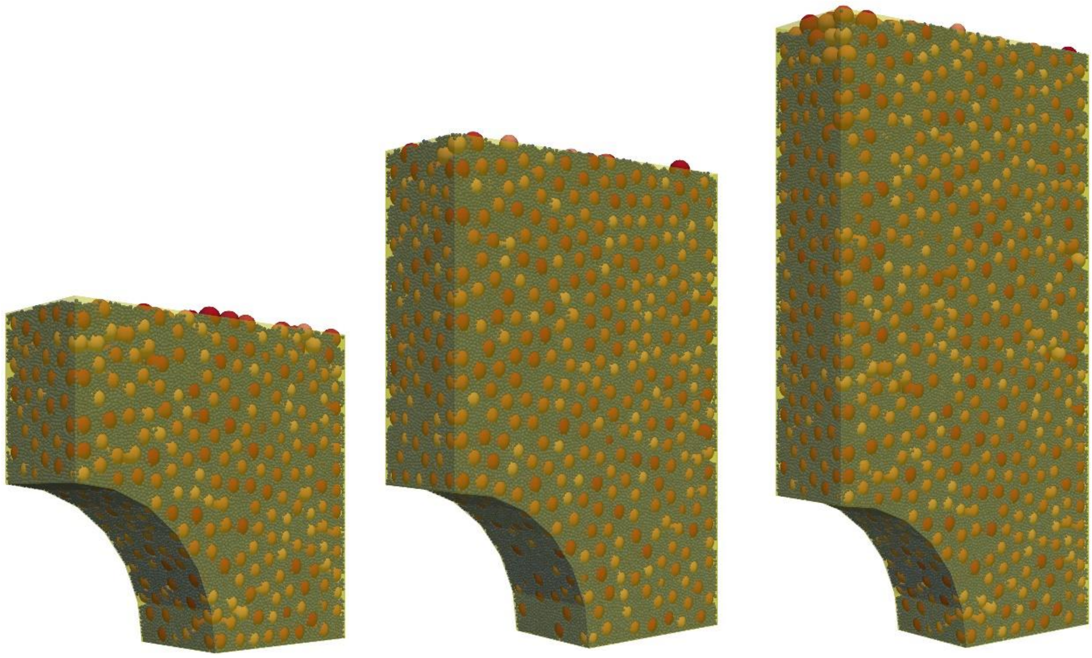

(a)Model-1 (f_r = 6, f_c = 25%, C/D=0.5) (b)Model-2 (f_r = 6, f_c = 25%, C/D=1.0) (c)Model-3 (f_r = 6, f_c = 25%, C/D=1.5)

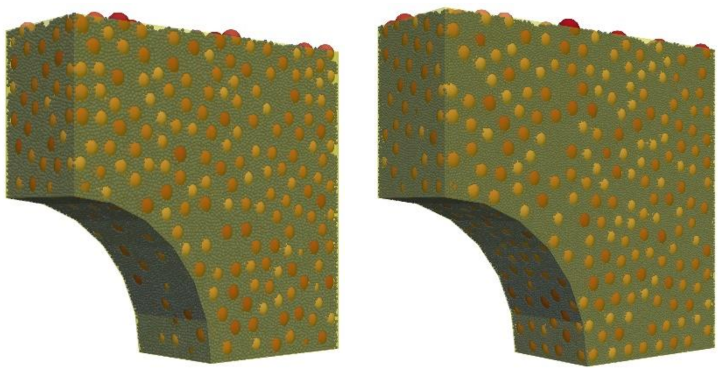

(d)Model-4 (f_r = 6, f_c = 35%, C/D=0.5) (e)Model-5 (f_r = 8, f_c = 25%, C/D=0.5)

Fig. 6.DEM Models after generation

The geometries and cells of three CFD computational domains corresponding to three different overburden-to-diameter ratios (C/D = 0.5, 1.0, 1.5) are shown in Fig. 7 and they respectively contain 13880, 21160 and 28440 cells, divided by structured hexahedron grids. In the fluid domain, the groundwater table was assumed to be at the ground surface and the water pressure was generated accordingly. The zero pressure boundary condition was applied to the crack to simulate the flow. Different values of constant underground water pressure were used corresponding to different buried depths of tunnel crack.

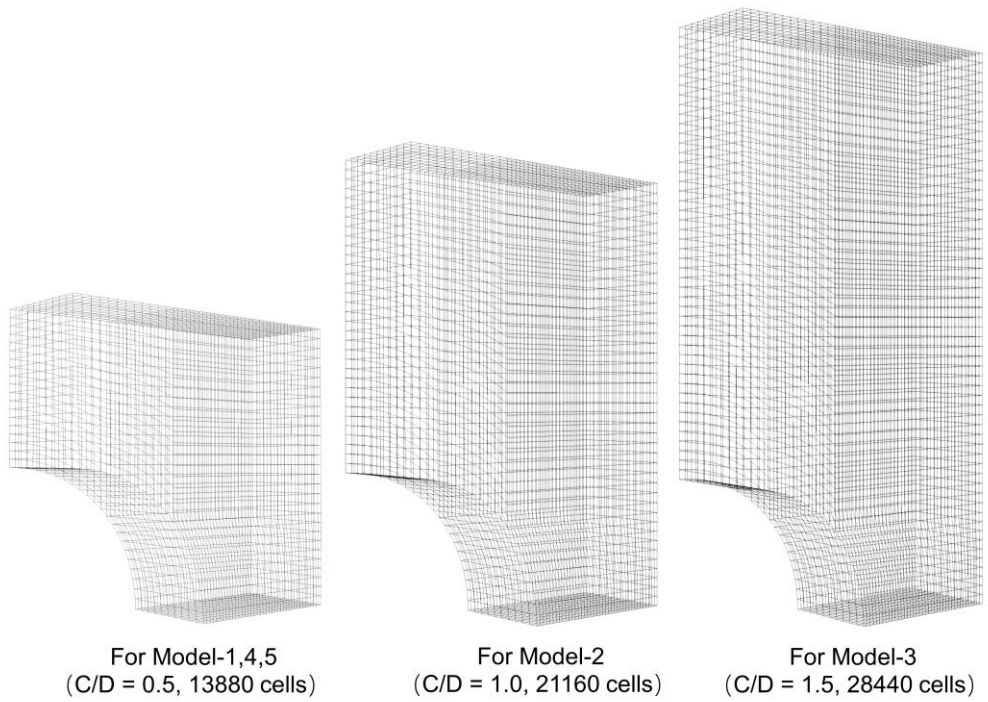

Fig. 7.CFD grids for all simulations

To get the distribution of fines content, void ratio and stress state, a few measurement columns (derived from measurement circles) were placed in each model. In order to get more accurate information, there are many overlaps between measure columns and the measure columns placed on the boundary of the models as shown in Fig. 8. The real distribution of measure columns in models is much denser than that shown in Fig. 8. The total number of measure columns is 183.

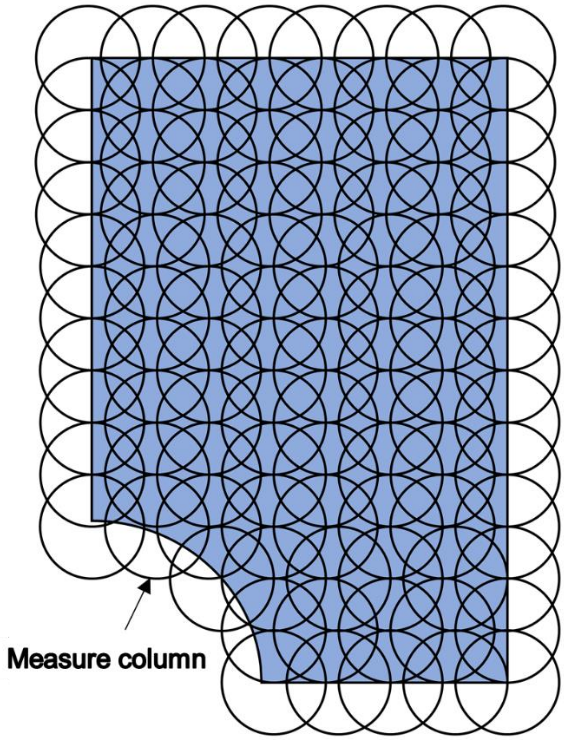

Fig. 8. Schematic diagram of measure columns

After the generation of the DEM model, the CFD-DEM coupling simulation started. The curved wall was replaced by the shorter one as shown in Fig. 5 to open the crack. The seepage erosion progress started, and particle migration was triggered. The migration was caused by both the gravity and seepage flow.

4. Results and discussion

4.1 Fines loss

The comparison of the temporal evolution of fines loss quantity in different models provides a direct way to investigate the difference in seepage erosion between these models. The progression of eroded particles percentage (mass ratio of the loss of fine particles to all fine particles) with time for all five models is presented in Fig. 9.(a). The fine particle loss in these five models were all induced by both gravity and flow field. To exclude the influence of gravity on the loss of fines, the progression of fine particle loss without hydraulic pressure for all models is shown in Fig. 9.(c) as a reference. The significant difference in fines loss between the two conditions confirms that seepage causes fines loss.

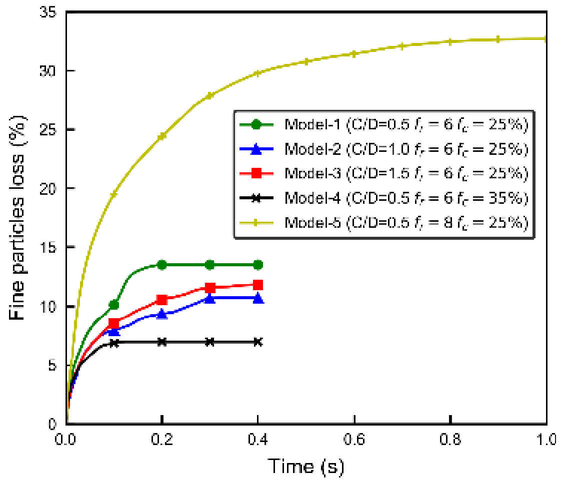

(a)

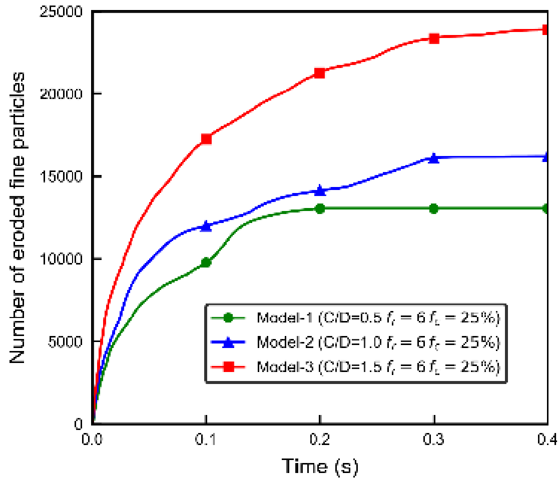

(b)

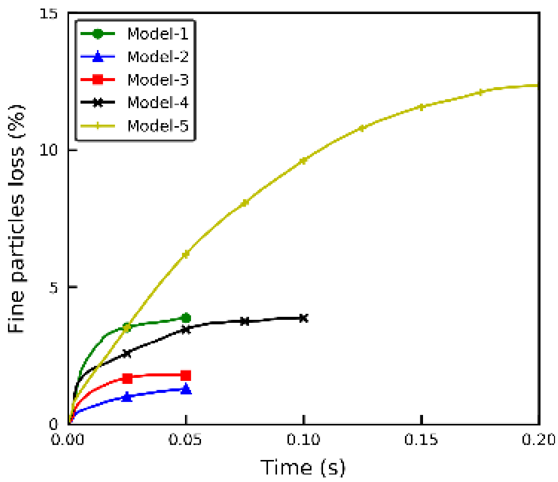

(c)

Fig. 9. Results of fins loss during seepage erosion: (a) percentage of fines loss versus time, (b) number of eroded fine particles versus time, and (c) percentage of fines loss due to only gravity versus time

For all five models, the fines loss increased rapidly with time at first and then the loss rate is gradually decreased until seepage erosion stabilized. This trend is in good agreement with the numerical simulation results (Zhang et al., 2019) and the experimental results (Rochim et al., 2017).

For Model-1, Model-2 and Model-3, which possess the same GSD and only differ in model size, it is more reasonable to compare the number of fines loss than to compare the percentage of loss. As shown in Fig. 9.(b), the number of eroded fines increases with the increase of buried depth.

By comparing the fines loss of model-1 and model-4, the fines loss for the model of larger fines content (f_c=35%) is much smaller than that of smaller fines content (f_c=25%). Fewer fines loss for the model of f_c=35% confirms that excessively high fines content would lead to a blockage between coarse particles (Wan and Fell, 2004). Moreover, Fig. 9.(a) shows the fines loss of model-5 (f_r=8) is about 3 times bigger than that of model-1 (f_r=6). The obvious difference in fines loss shows that the size ratio of coarse to fine particles has a significant effect on seepage erosion.

The spatial distribution of fines content and void ratio around the tunnel would change during the seepage erosion. Many researches put forward constitutive models for soils considering fines content (Yin et al., 2016b) and conducted FEM simulation with these models to simulate the seepage erosion around the tunnel (Yang et al., 2019c, 2019d). In these simulations, changes in the spatial distribution of fines content caused by seepage erosion often were presented as dominating results. As a numerical simulation method based on the microscopic mechanism with fundamentals of physics, CFD-DEM can simulate the variation of fines distribution from the basic principles of mechanics to provide more reliable results.

The distributions of fines content and the void ratio at the beginning and the end of the seepage erosion in the models are shown in Fig. 10 and Fig. 11. Seepage erosion leads to the decrease of the fines content especially around the crack. Comparing models with different buried depth (Model-1, Model-2, Model-3), it is found that the eroded zone increases with the buried depth. It could be directly attributed to the difference in the eroded fines mass of models with different buried depth. Compared to the model of f_c=25% (Model-1), the model of f_c=35% (Model-4) and the model of f_r=8 (Model-5) possess the smallest eroded zone and the largest eroded zone respectively.

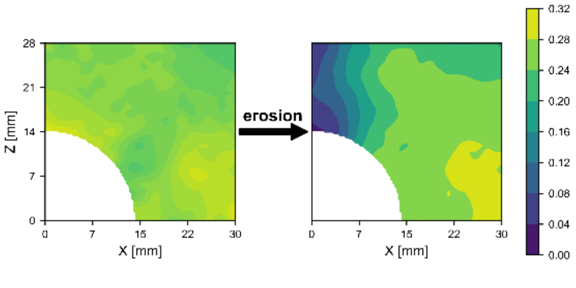

(a) Model-1 (f_r = 6, f_c = 25%, C/D=0.5)

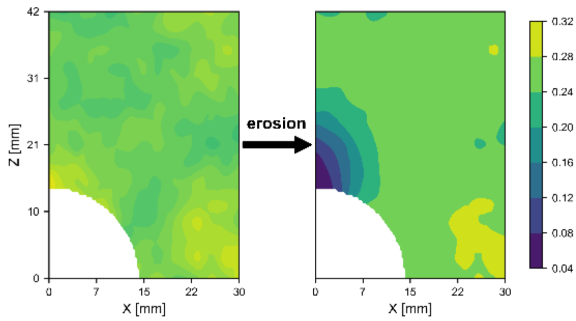

(b) Model-2 (f_r = 6, f_c = 25%, C/D=1.0)

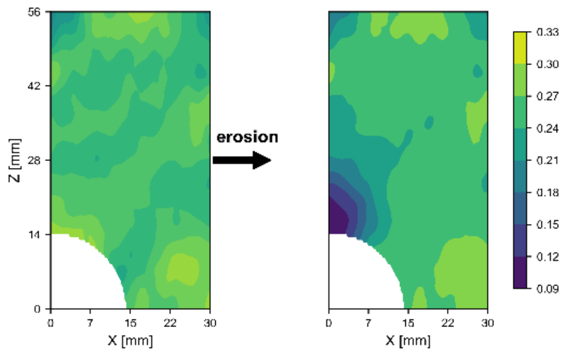

(c) Model-3 (f_r = 6, f_c = 25%, C/D=1.5)

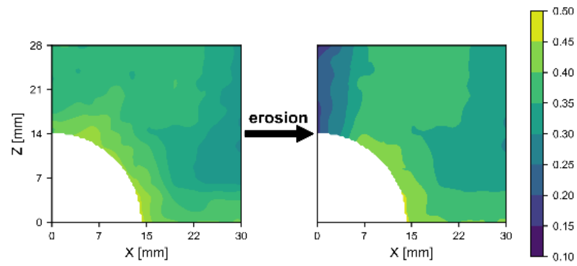

(d) Model-4 (f_r = 6, f_c = 35%, C/D=0.5)

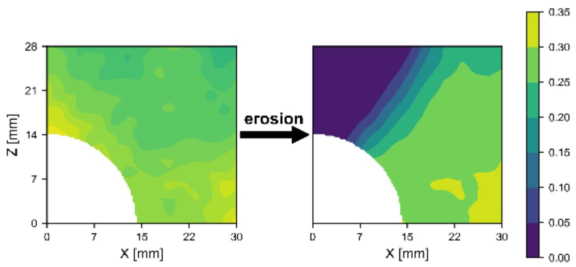

(e) Model-5 (f_r = 8, f_c = 25%, C/D=0.5)

Fig. 10. Field of fines content for all models before and after erosion

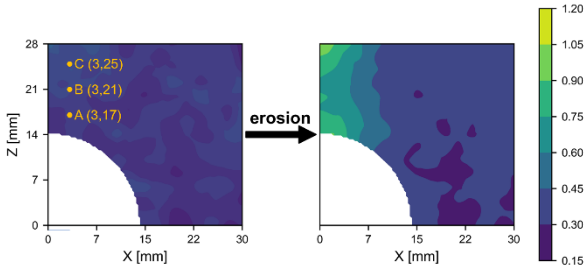

(a) Model-1 (f_r = 6, f_c = 25%, C/D=0.5)

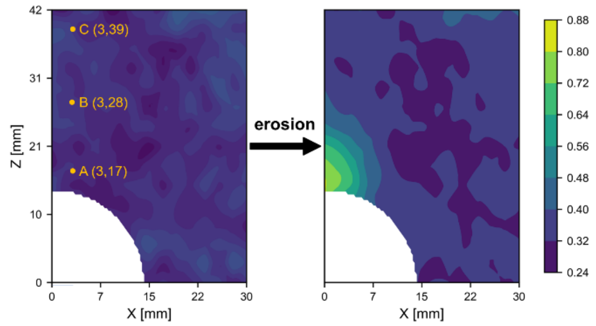

(b) Model-2 (f_r = 6, f_c = 25%, C/D=1.0)

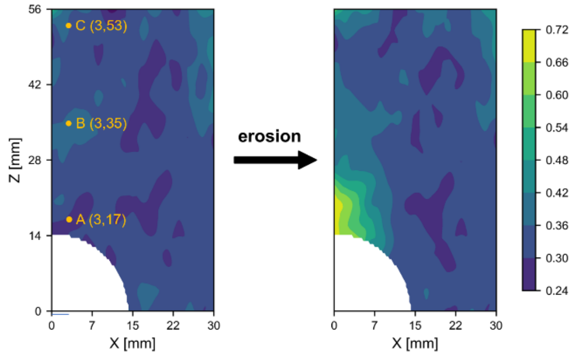

(c) Model-3 (f_r = 6, f_c = 25%, C/D=1.5)

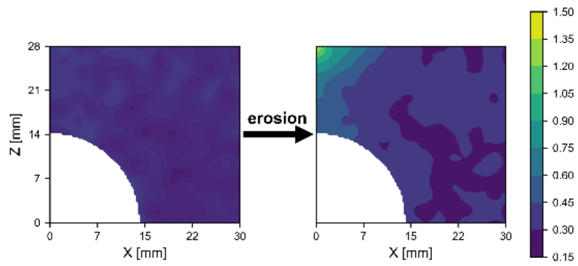

(d) Model-4 (f_r = 6, f_c = 35%, C/D=0.5)

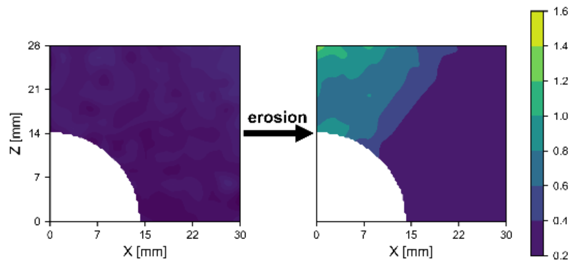

(e) Model-5 (f_r = 8, f_c = 25%, C/D=0.5)

Fig. 11. Field of void ratio for all models before and after erosion

The temporal evolution of the void ratio in different positions of the models would help to investigate the variation of void ratio in the complete process of seepage erosion. Fig. 12 presents the evolution of the void ratio for three measure points (equidistant distribution above the crack) in Models 1, 2 and 3 which vary in model size. The positions of the measure points are presented in Fig. 11. The void ratio at bottom points firstly grows and then tends to be stable. When the model is smaller, the growth rate difference of the void ratio among different points is less obvious. All three void ratio values in Model-1 show that the void ratio increases while the increasing rate decreases with height. In Model-2 and Model-3, the void ratio of top and middle points is almost unaffected by seepage.

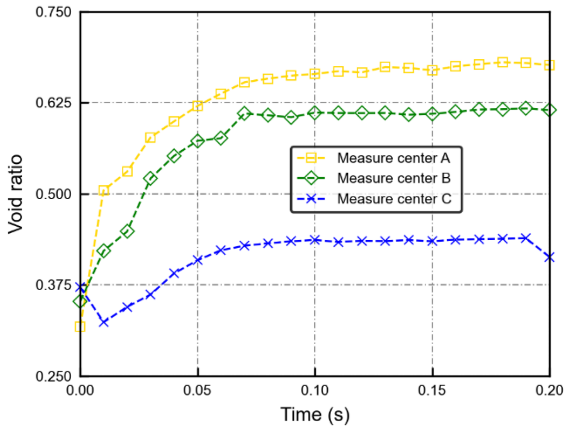

(a) Model-1

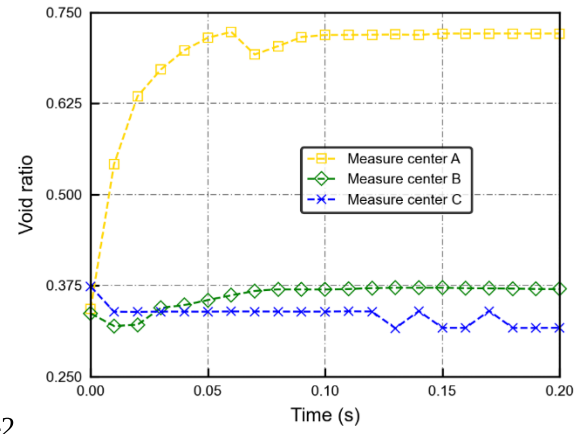

(b) Model-2

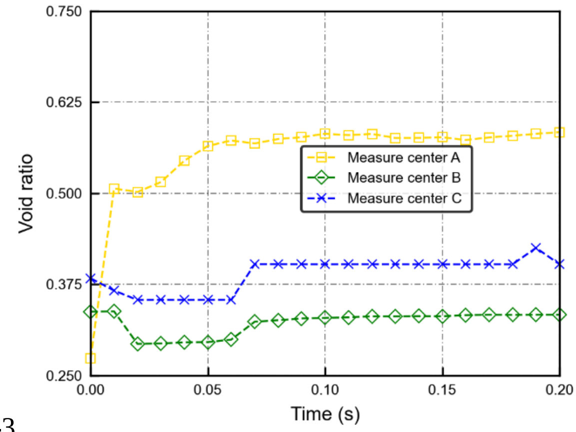

(c) Model-3

Fig. 12. Temporal evolution of void ratio at specific points in Models-1, 2 and 3

Fines loss in simulation consists of each individual eroded particle. The flow path of particles can be displayed with the aid of DEM, which helps us to better understand the process of particle mitigation from a microscopic insight.

In the models, the erodible fines were driven by fluid drag force and particle-particle contact force and flowed through the gap between coarse particles. To investigate the eroded particle movement under the hydraulic pressure and soil pressure, the flow paths in Model-3 (the largest model) of three eroded particles, initial positions of which are relatively far from the crack, are recorded and presented in Fig. 13. The positions of the particles were recorded every 10000 steps (0.001s). Dense points in the flow path indicate that the particle flowed slowly and even was blocked. Whilst loose points indicate that the particle flowed rapidly without obstruction. Three modes of particle flow in the process of seepage (i.e. detachment, transport and filtration) can be observed in Fig. 13. It can also be seen that three modes appeared alternately in one particle's eroded path.

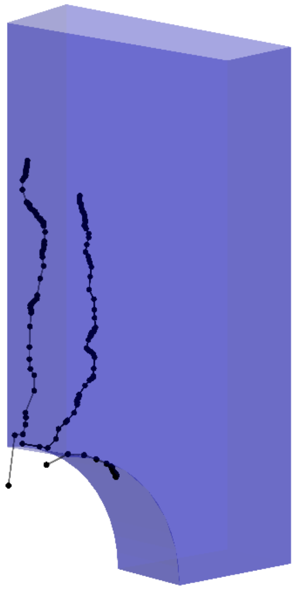

Fig. 13. Flow path of the selected eroded particles

4.2 Ground settlement

As mentioned earlier, seepage erosion causes fines loss. Both the fines loss-induced mass and modulus reduction would induce the ground settlement. Seepage erosion-induced ground settlement in the five models are plotted in Fig. 14. Like previous studies (Zhang et al., 2012), the settlement decreases with the increase of the distance from the center of the tunnel. And the settlement increases with the loss of fines except for the Model-4 with an initial fines content of 35%. This phenomenon can be explained as follows: with bigger initial fines content, more fines would cause more separation of coarse particles by fines. When the fines which blocked the contact between the coarse particles were eroded, the coarse particles would move and then more settlement would be induced. A similar result can be found in (Ouyang and Takahashi, 2015). When the initial fines content increases from 25% to 35%, the volumetric strain grows sharply.

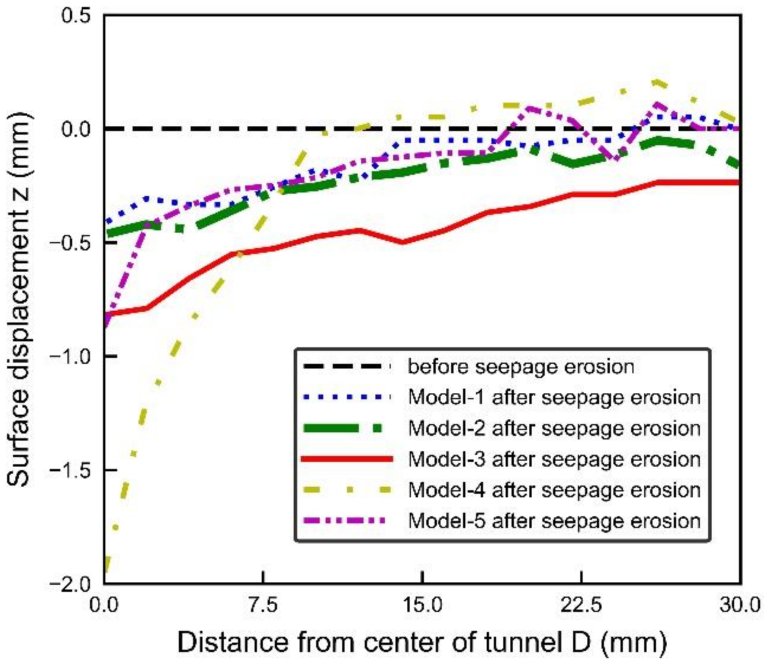

Fig. 14. Ground settlement induced by seepage erosion in five models

The models at the end of the test are shown in Fig. 15 as references. The color of particles in the model represents the particle position before the seepage erosion for better visualization. Fig. 15 shows that the fines tend to flow over long distances. Even the fines at ground level in model-1 and model-5 were washed away. In model-2 and model-3, we can observe that some of the fines originally in the upper part of the model also flowed for a long distance towards the direction of the crack.

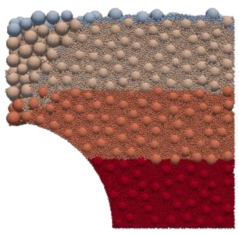

(a) Model-1 (f_r = 6, f_c = 25%, C/D=0.5)

(b) Model-2 (f_r = 6, f_c = 25%, C/D=1.0)

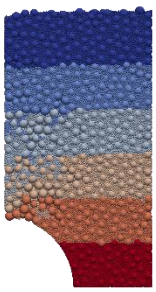

(c) Model-2 (f_r = 6, f_c = 25%, C/D=1.5)

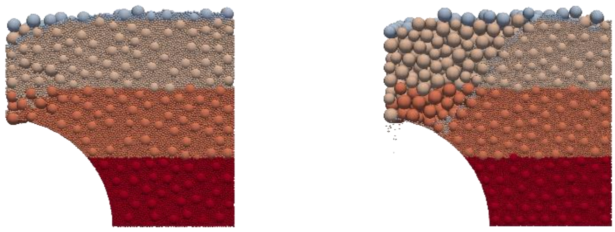

(d) Model-4 (f_r = 6, f_c = 35%, C/D=0.5) (e) Model-5 (f_r = 8, f_c = 25%, C/D=0.5)

Fig. 15. DEM Models after seepage erosion

4.3 Stress redistribution

The stress distribution around the tunnel change with the loss of particles and fabric variation during the seepage erosion. And the variation of earth pressure acting on tunnel segments is crucial for the safety of tunnels in engineering practice. The pressure acting on the one-quarter of tunnels in the models before seepage erosion and at the end of seepage erosion is shown in Fig. 16.

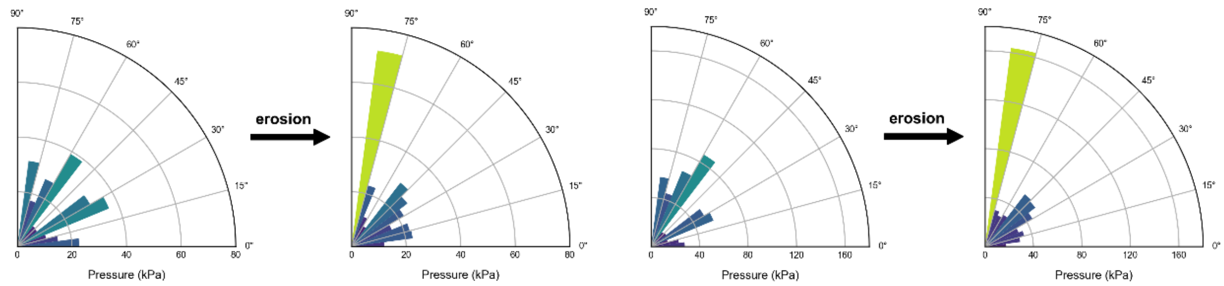

(a) Model-1 (f_r = 6, f_c = 25%, C/D=0.5) (b) Model-2 (f_r = 6, f_c = 25%, C/D=1.0)

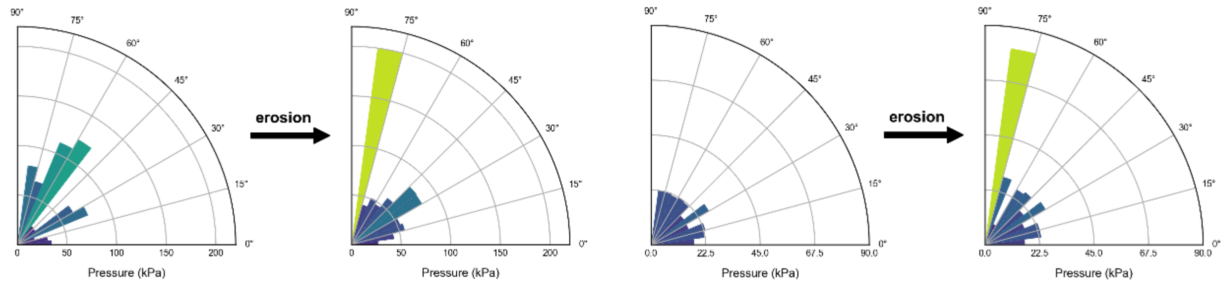

(c) Model-3 (f_r = 6, f_c = 25%, C/D=1.5) (d) Model-4 (f_r = 6, f_c = 35%, C/D=0.5)

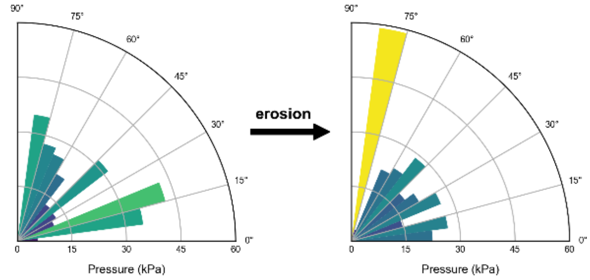

(e) Model-5 (f_r = 8, f_c = 25%, C/D=0.5)

Fig. 16. Earth pressure acting on the curved wall before and after seepage erosion

The change of soil pressure acting on the tunnel lining is mainly caused by the transformation of the particle-particle force structure induced by the loss of fines. When the seepage erosion began, the earth pressure acting on the position of the crack is decreased sharply and the coarse particles around the crack formed a force arch to bear the earth pressure. The arch springing was on both sides of the crack thus the earth pressure aside of the crack is increased, which can be observed in Fig. 16. The increase of earth pressure near the crack after seepage erosion occurred on all five models. Moreover, the earth pressure near the crack increases with the buried depth but it does not change dramatically with the GSD. Comparing the pressure near the crack for Model-1, Model-4 and Model-5 (72.01 kPa, 81.06 kPa and 58.93 kPa separately), it can be inferred that the redistribution degree of soil pressure acting on the tunnel lining increases with fines content and decreases with mean particle size ratio. At the same time, the segment near the crack is usually the weakest part of tunnels. Therefore, the increase of earth pressure near the crack would most likely widen the crack and then induced more loss of fine particles to form a vicious circle.

Since the earth pressure is determined from vertical and horizontal stresses around the tunnel, the vertical and horizontal stresses (σ_z, σ_x) distributions in these five models before and after erosion are also presented in Fig. 17 and Fig.18 as a reference. The average stress tensor in the measure column is calculated by Eq.(8):

$$\sigma_{ij} = \frac{1}{V}\sum_{1}^{C}(R_1 + R_2)Nn_in_j + \frac{1}{V}\sum_{1}^{C}(R_1 + R_2)Tn_it_j\left(n_it_i = 0\right) \quad (8)$$

where V is the volume of measure column, C is the contacts in the volume, R_1 and R_2 is the diameter of the two touching particles, N and T are the magnitudes of the normal and tangential contact forces, n_i is the unit vector normal to the contact plane and t_i is the unit vector parallel to the contact plane. Note that σ_{xx} and σ_{zz} correspond to the horizontal and vertical stresses, respectively.

Stresses (σ_z, σ_x) in the area above the crack was redistributed most violently in all the five models. The area where significant redistribution occurs expands with the increase of the model size. Model-5 with a bigger mean particle size ratio shows a greater degree of stress redistribution.

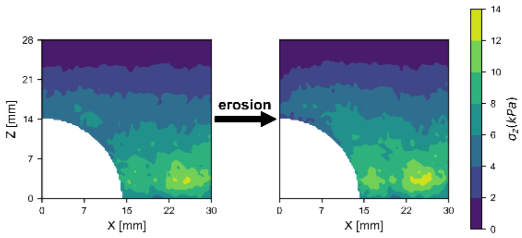

(a) Model-1 (f_r = 6, f_c = 25%, C/D=0.5)

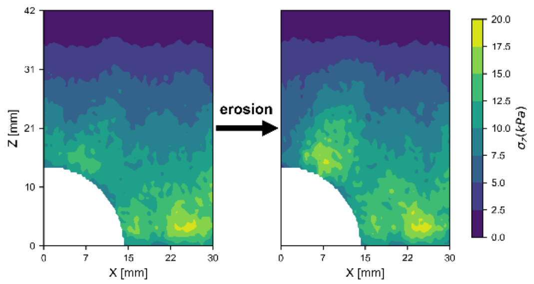

(b) Model-2 (f_r = 6, f_c = 25%, C/D=1.0)

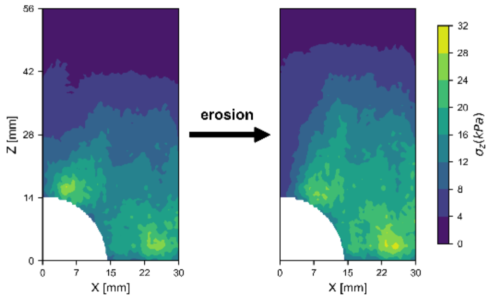

(c) Model-3 (f_r = 6, f_c = 25%, C/D=1.5)

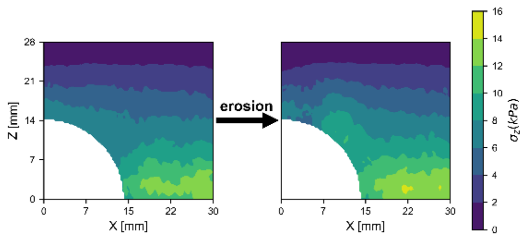

(d) Model-4 (f_r = 6, f_c = 25%, C/D=0.5)

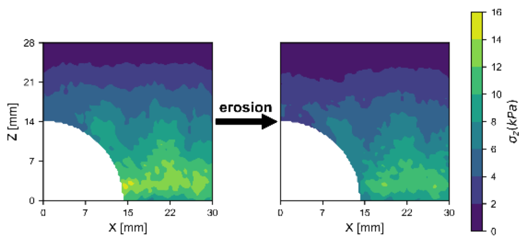

(e) Model-5 (f_r = 8, f_c = 25%, C/D=0.5)

Fig. 17. Field of vertical stress for all models before and after erosion

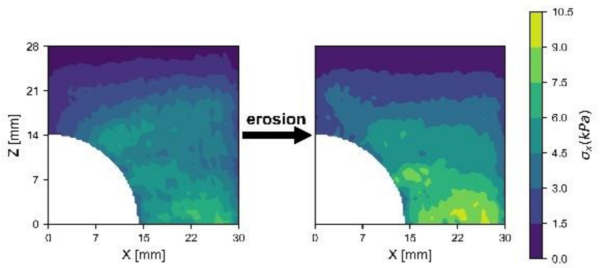

(a) Model-1 (f_r = 6, f_c = 25%, C/D=0.5)

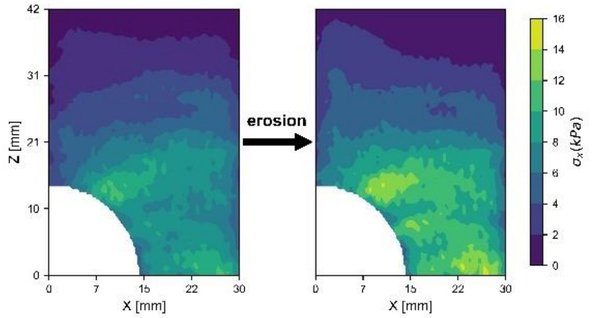

(b) Model-2 (f_r = 6, f_c = 25%, C/D=1.0)

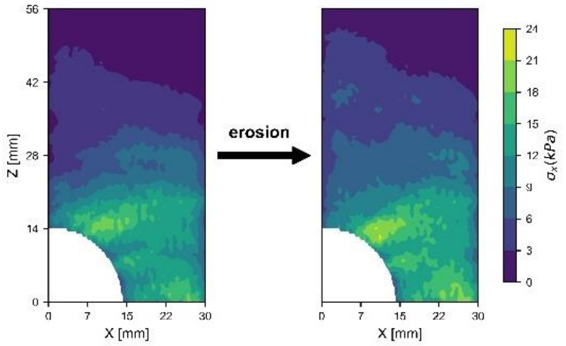

(c) Model-3 (f_r = 6, f_c = 25%, C/D=1.5)

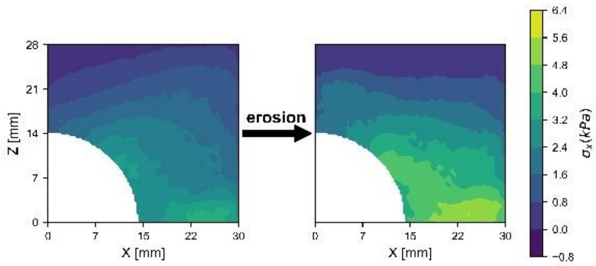

(d) Model-4 (f_r = 6, f_c = 35%, C/D=0.5)

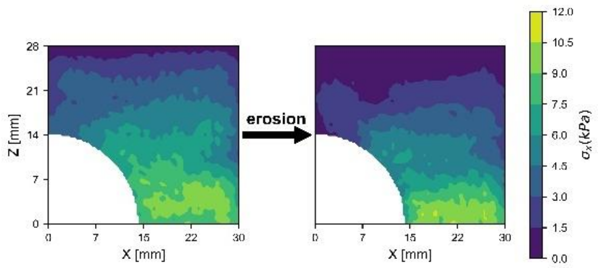

(e) Model-5 (f_r = 8, f_c = 25%, C/D=0.5)

Fig.18. Field of horizontal stress for all models before and after erosion

4.4 Analysis of micromechanics and microstructure

With the aid of DEM, information of each contact can be collected. The analyses of microscopic structure would be helpful to investigate the variation of the models during the seepage erosion. To observe the evolution of contact fabric during the seepage erosion in the five models, the contact force for these models are analyzed, shown in Fig. 19. The cylinders in the figures denote the contact force, which links the centroid of adjacent particles, thus the contact types (coarse-coarse, fine-fine, fine-coarse) can be distinguished by the length of the cylinders. The radius (or thickness) and color of the cylinders represent the magnitude of the force. Before the seepage erosion, the contact force is gradually increased with depth and was distributed uniformly in the horizontal direction. After the seepage erosion, the contact force around the tunnel crack is increased and the distribution of contact force becomes heterogeneous. Similar to Fig. 17 and Fig.18, the area where the distribution and shape of the force chain increases significantly with the model size. Comparing Model-1 and Model-4, larger fines content (f_c=35%) leads to a more uniform distribution of force chain whether before or after seepage erosion. In Model-5 (f_r=8), seepage erosion leads to the disappearance of a large number of force chains while the force chains around the crack are more uniform compared to those of Model-1 (f_r=6).

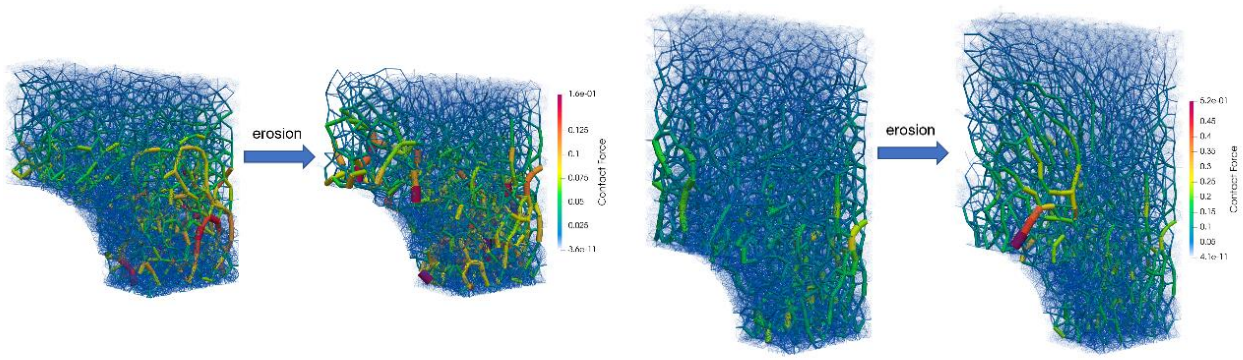

(a) Model-1 (f_r = 6, f_c = 25%, C/D=0.5) (b) Model-2 (f_r = 6, f_c = 25%, C/D=1.0)

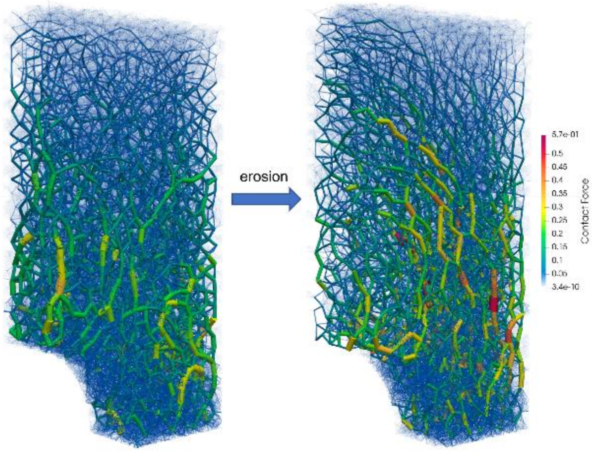

(c) Model-3 (f_r = 6, f_c = 25%, C/D=1.5)

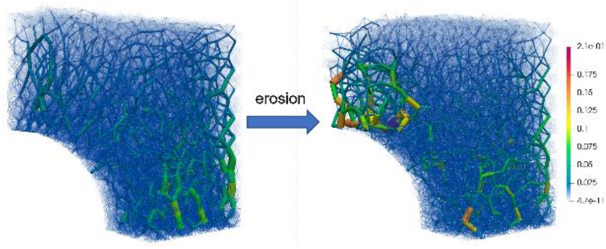

(d) Model-4 (f_r = 6, f_c = 35%, C/D=0.5)

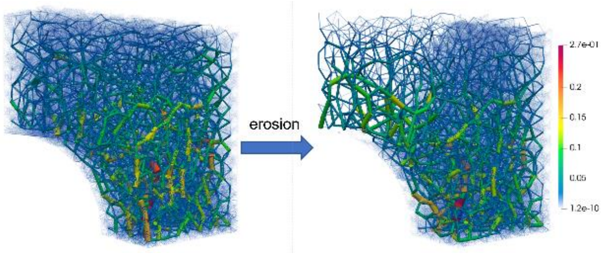

(e) Model-5 (f_r = 8, f_c = 25%, C/D=0.5)

Fig. 19. Force chains of all models before and after erosion

Furthermore, the variation of fabric anisotropy is usually used to analyze the contact fabric of granular materials. Some parameters are calculated to measure the degree of anisotropy in previous studies to investigate the evolution of fabric anisotropy quantitatively (Gu et al., 2018, 2015, 2014a). In these models, the sharpest changes of stress, fines content and void ratio occurred in the area above the crack. Thus, the contact information in the area (Fig. 20) were collected to calculate the anisotropy parameters. Fig. 21 shows the change of the 3D angular distribution of contact normal, normal contact force and shear contact force of Model-5 as an example. The scalar anisotropy parameters α_r, α_n and α_t were estimated to quantify the anisotropy degree of distribution of contact normal, normal contact force and shear contact force respectively. The definition of the three parameters are briefly described below.

A second-order fabric tensor (Rothenburg and Bathurst, 1989; Sitharam et al., 2002) which is from the statistics of spatial distribution of contact normal is introduced here. The fabric tensor is defined as follows:

$$R_{ij} = \int_{\Omega} E(\Omega) n_i n_j d\Omega = \frac{1}{N} \sum_{c \in N} n_i n_j \quad (9)$$

where n_i is the unit contact normal in the i-direction, N is the total number of contacts, and $E(\Omega)$ is the distribution function on the unit sphere Ω.

Similarly, the distribution of normal contact force and tangential contact force in space can also be expressed by second-order tensor as follows (Gu et al., 2014b; Guo and Zhao, 2013):

$$F_{ij}^{n} = \frac{1}{4\pi} \int_{\Omega} \overline{f}^{n}(\Omega) n_i n_j d\Omega = \sum_{c \in N} \frac{f^{n} n_i n_j}{N\left(1 + a_{kl}^{r} n_k n_l\right)} \quad (10)$$

$$F_{ij}^{t} = \frac{1}{4\pi} \int_{\Omega} \overline{f}^{t}(\Omega) t_i n_j d\Omega = \sum_{c \in N} \frac{f^{t} t_i n_j}{N\left(1 + a_{kl}^{r} n_k n_l\right)} \quad (11)$$

where $\bar{f}^{n}(\Omega)$ and $\bar{f}^{t}(\Omega)$ are the spatial distributions of normal contact force and shear contact force respectively and a_{ij}^{r} is the second-order anisotropy tensor of contact normal, which can be deduced from the deviation of fabric tensor ($R_{ij}^{\prime}$)

$$a_{ij}^{r} = \frac{15}{2} R_{ij}^{\prime} \quad (12)$$

And then scalar anisotropy parameters are used to quantify the degree of contact normal anisotropy (Gu et al., 2014b; Guo and Zhao, 2013; Sitharam et al., 2002):

$$a_{r} = \sqrt{\frac{3}{2} a_{ij}^{r} a_{ij}^{r}} \quad (13)$$

Similarly, two other parameters a_n and a_t are used to quantify normal contact force and shear contact force anisotropy:

$$a_{ij}^{n} = \frac{15}{2} F_{ij}^{n'} / \overline{f}_{0}^{n} \quad (14)$$

$$a_{ij}^{t} = 5 F_{ij}^{t'} / \overline{f}_{0}^{n} \quad (15)$$

$$a_{n} = \sqrt{\frac{3}{2} a_{ij}^{n} a_{ij}^{n}} \quad (16)$$

$$a_{t} = \sqrt{\frac{3}{2} a_{ij}^{t} a_{ij}^{t}} \quad (17)$$

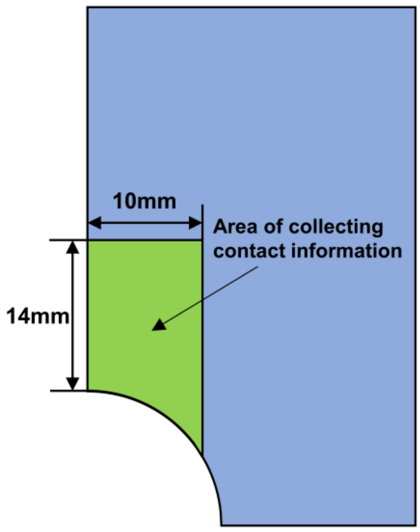

Fig. 20. Selected area for collecting contact information

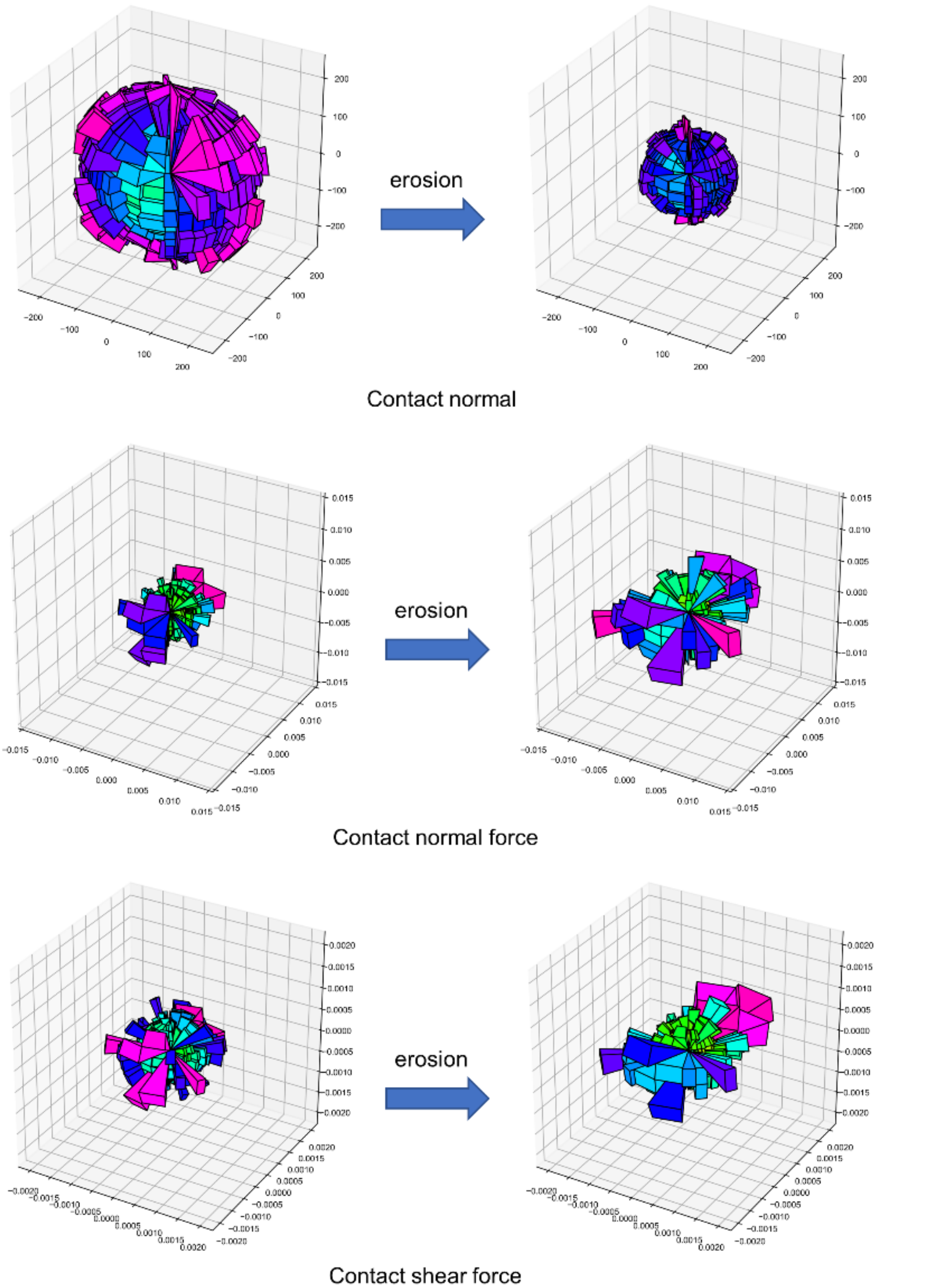

Fig. 21. Three-dimensional angular distribution for contact normal, normal contact force and shear contact force of model-5 before and after erosion

The change of the anisotropy parameters of the five models is shown in Fig. 22. The value of α_r is small with a slight change in Model-1, 2 and 3, while both the initial value and variation trend of α_r are much influenced by the GSD comparing the case of f_c = 25% to that of f_c = 35%. It can be observed that the initial value of α_r in Model-1, 4 and 5 differs with each other obviously, and α_r decreases with seepage erosion in Model-4 while increases in Model-5. The α_n value decreases with seepage erosion in all five models. This phenomenon can be explained by the stress redistribution. Because the soil in the model is in the K_0 stress state before seepage, the direction of the major principal stress is vertical, so there is a certain initial anisotropy of normal and tangential contact forces in each model. The initial a_n of each model is large. After the seepage, the upper part of the crack is lost and the upper force chain tends to be arched to carry the upper part of the soil, which makes the contact force in the horizontal direction larger, resulting in a significant decrease in both a_n and a_t. Fig. 19 shows that the main strong contacts are vertically distributed before seepage, and strong horizontal strong contacts appear around the cracks of each model after seepage. Meanwhile, the a_n of Model-5 decreases the least before and after seepage in each model, which corresponds to the lowest Model-5 pressure in the segment around the crack after seepage. Comparing to the extent of decrease in Model-1, more fines (Model-4) lead to a greater reduction of α_n, while greater mean particle size ratio causes an inconspicuous decline.

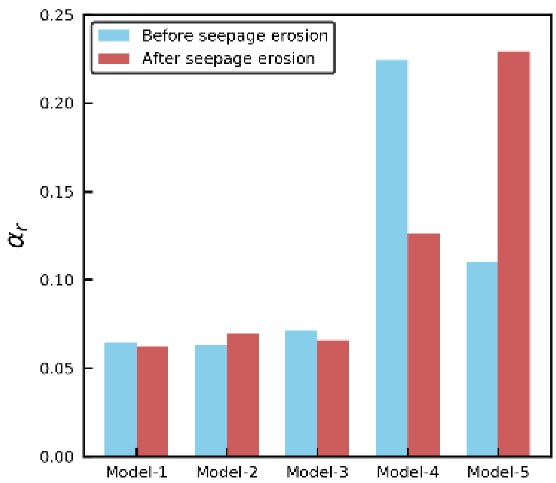

(a)fFor contact normal

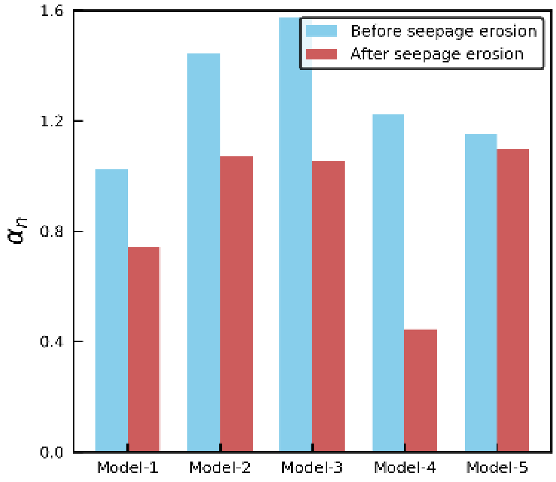

(b) for normal contact force

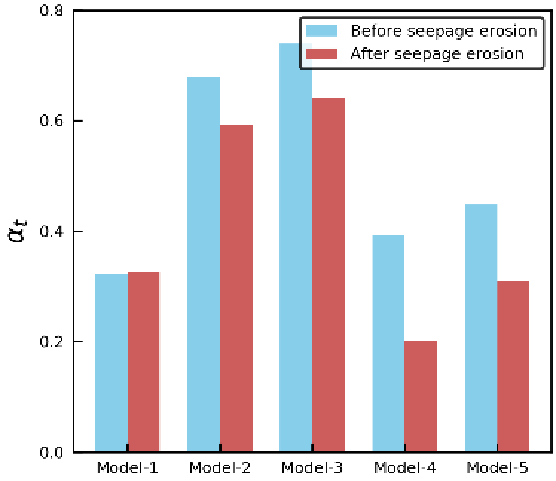

(c) for shear contact force

Fig. 22. Anisotropy parameters before and after erosion

4.5 **Variation of soil mechanical properties**

As mentioned earlier, seepage erosion induced the decrease of fines content and the increase of void ratio near the crack. The variations of fines content and void ratio could significantly affect the mechanical behavior, such as strength, modulus and position of the critical state line (Yin et al., 2016b, 2014). In the actual engineering case, the change of strength and deformation characteristics of soils caused by seepage may lead to a variety of engineering disasters, such as settlement, sinkhole and so on. To investigate these changes in detail, the strength and deformation characteristics of the soil near the cracks before and after seepage were tested.

Void ratio and fines content in the calculation area (as seen in Fig. 20) in five models were calculated and summarized in Table 3. Ten cubic samples with the same void ratio and fines content as those of the five models before and after erosion were prepared. The method of making a sample with a specific initial void ratio is referred to Gu (2014a). That is, to control the inter-particle friction coefficient in the process of packing in two stages, and continuously adjust the inter-particle coefficient until a sample with a specified void ratio is produced. The confining pressure in the triaxial tests is the average pressure in the corresponding tunnel model. For example, buried depth ratios of 0.5, 1.0, 1.5 correspond to confining pressures of 9kPa, 27kPa, 45kPa respectively. The results of triaxial loading tests on these ten samples are shown in Fig. 23. All the five samples before erosion show shear dilatancy while after erosion they exhibit shrinkage due to the loss of fines as well as the increase in void ratio. To investigate the influences of buried depth and GSD on deformation stiffness and shear strength, the peak stress ratio difference and the ratio of E_{50} (defined as the initial slope of the deviatoric stress corresponding to half of the peak strength to the axial strain) before and after erosion are presented in Fig. 24. In all the five pairs, the peak stress ratio and the stiffness generally decrease due to internal erosion. The stress ratio difference of Model-4 (f_c = 35%) and the ratio of E_{50} of Model-5 (f_r = 8) are significantly larger than those of other models.

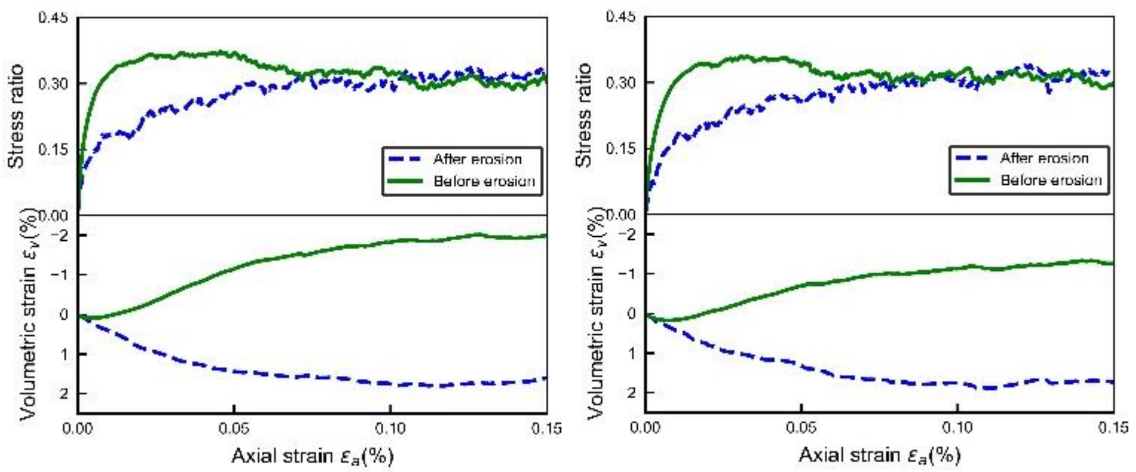

(a) Model-1 (f_r = 6, f_c = 25%, C/D=0.5) (b)Model-2 (f_r = 6, f_c = 25%, C/D=1.0)

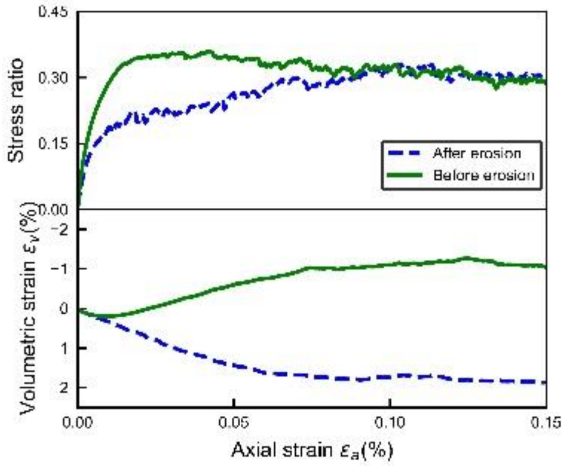

(c) Model-3 (f_r = 6, f_c = 25%, C/D=1.5)

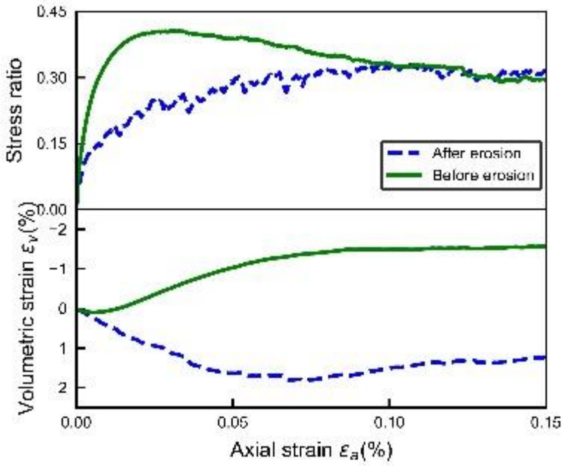

(d) Model-4 (f_r = 6, f_c = 35%, C/D=0.5)

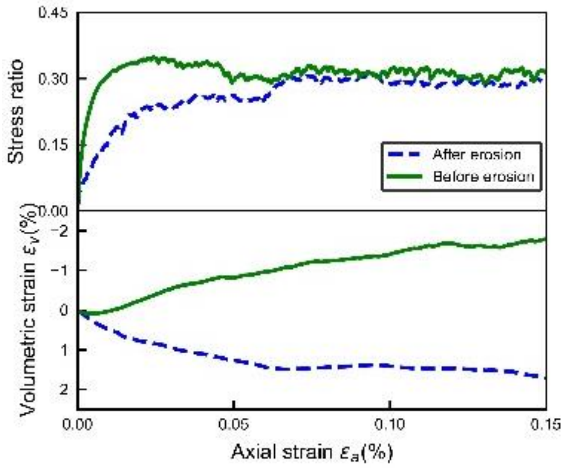

(e)Model-5 (f_r = 8, f_c = 25%, C/D=0.5)

Fig. 23. Changes of strength and deformation characteristics expressed by stress ratio (deviatoric stress over mean effective stress) versus axial strain and volumetric strain versus axial strain caused by erosion for all models

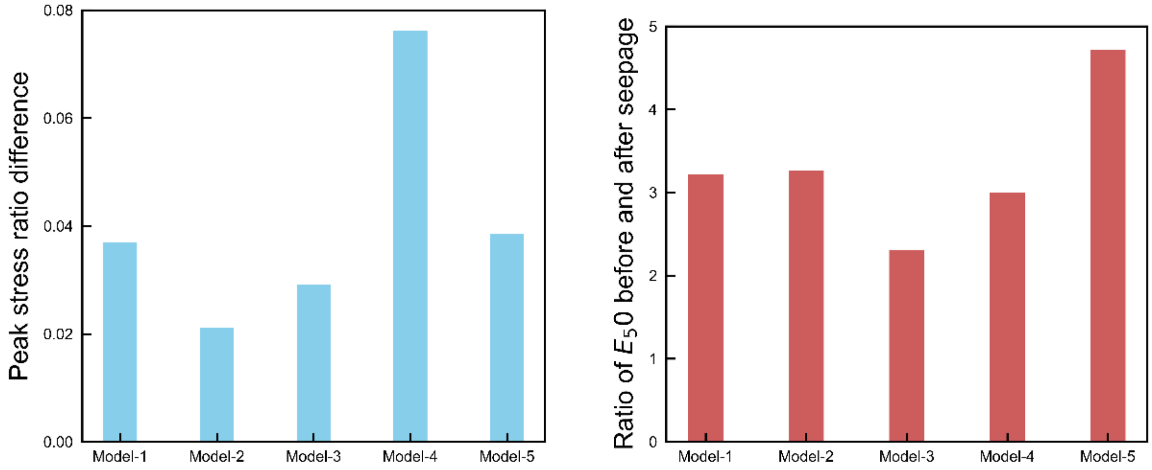

(a) (b)

Fig. 24. Stress ratio difference and stiffness ratio before to after erosion in the five models

Table 3 Fines content and void ratio after erosion in the calculation area

Model No.	After erosion	
	Fines content, f_c	Void ratio, e
Model-1	15%	0.529
Model-2	17.4%	0.532
Model-3	13.2%	0.552
Model-4	23.6%	0.432
Model-5	0.459%	0.766

To estimate the movement of the critical state line, triaxial tests were carried out on 15 samples, summarized in Table 4. Five kinds of combinations of specific f_c and e were selected corresponding to all models, and "f_c = 0" is a specific reference sample. Three confining pressures (9 kPa, 27 kPa, 45 kPa) were adopted for triaxial test simulations. The information about the critical state of the above 15 samples is shown in Fig. 25. The movement of critical state line induced by seepage erosion, or rather fines loss is confirmed. The degree of movement is affected by GSD of samples.

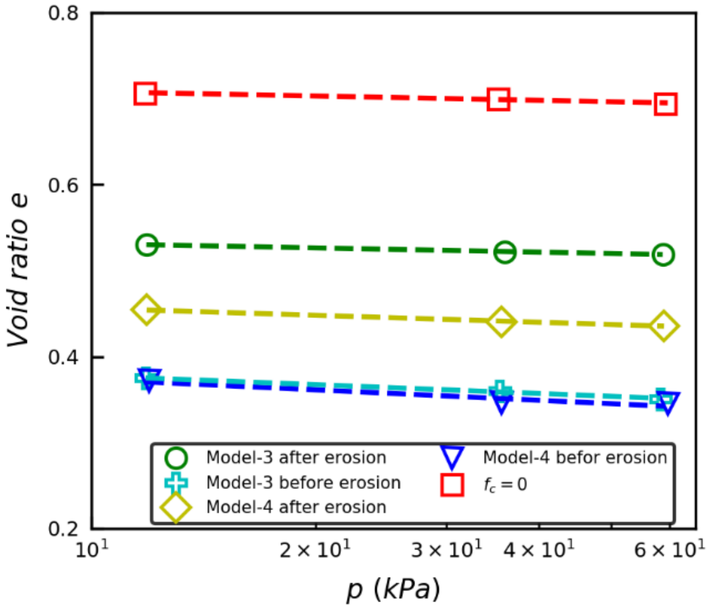

Fig. 25. Critical state lines in e-logp' plane for soils of different fines contents from models before or after erosion

Table 4 Summary information of 15 samples for triaxial tests

Corresponding Model	Fines content, f_c	Void ratio, e	Confining Pressure
Model-3 after erosion	13.2%	0.552	9 kPa, 27kPa, 45kPa
Model-3 before erosion	25%	0.337	9 kPa, 27kPa, 45kPa
Model-4 after erosion	23.6%	0.432	9 kPa, 27kPa, 45kPa
Model-4 before erosion	35%	0.351	9 kPa, 27kPa, 45kPa
"$f_c = 0$"	0%	0.729	9 kPa, 27kPa, 45kPa

4.6 Pore pressure around tunnel

The pore pressure distribution in the soil around the tunnel after seepage in different models is shown in the Fig. 26. The pore pressure around the tunnel is significantly reduced due to the influence of tunnel seepage: the closer to the crack position, the more the pore pressure decreases. The degree of this decrease in pore pressure is gradually increasing over time until stable. The temporal evolution of pore pressure in different models differs slightly from each other but with the same trend.

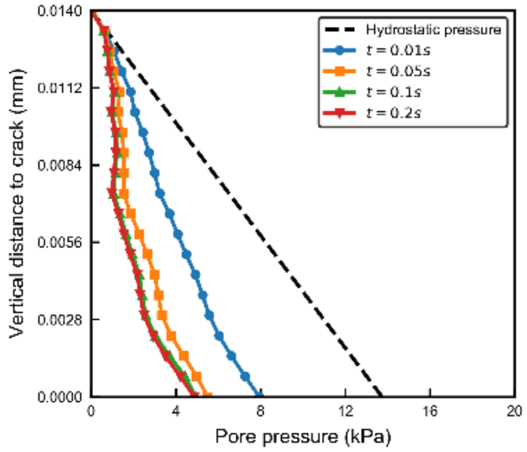

(a) Model-1 (f_r = 6, f_c = 25%, C/D=0.5)

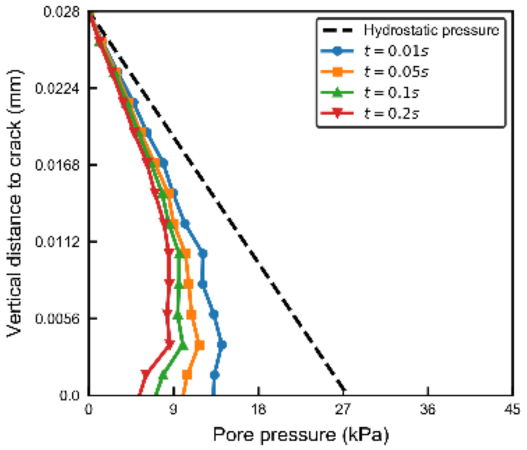

(b)Model-2 (f_r = 6, f_c = 25%, C/D=1.0)

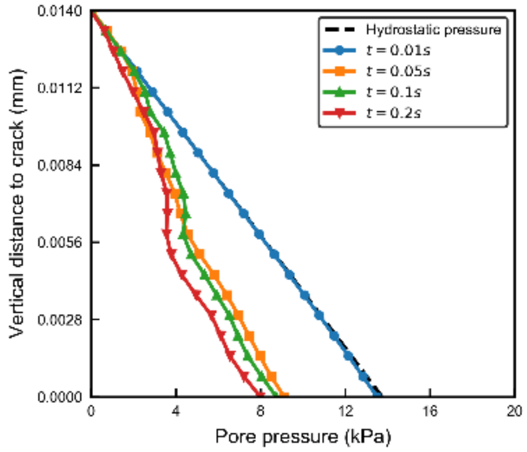

(c) Model-3 (f_r = 6, f_c = 25%, C/D=1.5)

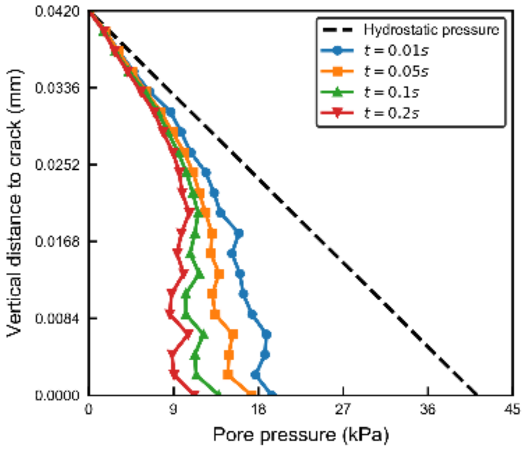

(d) Model-4 (f_r = 6, f_c = 35%, C/D=0.5)

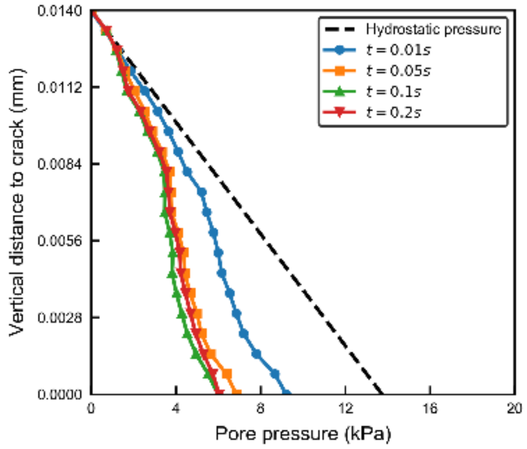

(e)Model-5 (f_r = 8, f_c = 25%, C/D=0.5)

Fig. 26. Profile of the pore pressure along with the depth above the tunnels during seepage erosion for all models

5. Conclusion

A CFD-DEM model was established for the seepage erosion in gap graded granular soils around the shield tunnel. The influences of the buried depth and GSD of soils have been investigated. The evolution of fines loss, ground settlement, stress redistribution, fabric anisotropy, mechanical property, pore pressure during the seepage erosion were analyzed. Both macro and micro results were discussed simultaneously to improve the understanding of seepage erosion around the tunnel. The key findings are summarized as follows:

(1) The loss of fines through cracks around tunnels is induced by both soil pressure and seepage drag force. The number of fines loss and the eroded zone increase with buried depth. Fewer fines loss occurs in a model with more fines content, and more fines loss is found in a model with a bigger mean particle size ratio.

(2) The ground settlement increases with buried depth. The model with a fines content of 35% possesses the maximum vertical displacement. A bigger settlement is found in the model with a bigger mean particle size ratio.

(3) The earth pressure near the crack significantly increases due to the stress redistribution induced by fines loss. The redistribution degree of earth pressure acting on the tunnel lining increases with fines content and decreases with mean particle size ratio. The stress redistributed area expands with buried depth.

(4) Similar to stresses distribution, the significantly varying area of force chains expands with buried depth. The GSD influences the form of force chains. The buried depth has a slight effect on the changes of microscopic parameters while GSD shows a significant impact on them.

(5) Mechanical properties such as the strength, deformability and the critical state of granular soils under the crack would encounter great change during the seepage erosion process. Both the strength and stiffness of soils around the crack decrease after the seepage erosion.

The above results can also provide evidence for further development of a continuous approach to solve real engineering scale problems of tunneling and underground space.

Acknowledgement

The financial supports provided by the GRF project (Grant No. 15209119) and FDS project (Grant No. UGC/FDS13/E06/18) from Research Grants Council (RGC) of Hong Kong are gratefully acknowledged.

References

Chand, R., Khaskheli, M.A., Qadir, A., Ge, B., Shi, Q., 2012. Discrete particle simulation of radial segregation in horizontally rotating drum: Effects of drum-length and non-rotating end-plates. Phys. A Stat. Mech. its Appl. 391, 4590–4596.

Chang, C.S., Yin, Z.-Y., 2011. Micromechanical modeling for behavior of silty sand with influence of fine content. Int. J. Solids Struct. 48, 2655–2667.

Cheng, K., Wang, Y., Yang, Q., 2018. A semi-resolved CFD-DEM model for seepage-induced fine particle migration in gap-graded soils. Comput. Geotech. 100, 30–51.

Cundall, P.A., Strack, O.D.L., 1979. A discrete numerical model for granular assemblies. geotechnique 29, 47–65.

ERGUN, S., 1952. Fluid flow through packed columns. Chem. Eng. Prog. 48, 89–94.

Fox, G.A., Wilson, G. V, Periketi, R.K., Cullum, R.F., 2006. Sediment transport model for seepage erosion of streambank sediment. J. Hydrol. Eng. 11, 603–611.

Gidaspow, D., Bezburuah, R., Ding, J., 1991. Hydrodynamics of circulating fluidized beds: kinetic theory approach.

Goniva, C., Kloss, C., Deen, N.G., Kuipers, J.A.M., Pirker, S., 2012. Influence of rolling friction on single spout fluidized bed simulation. Particuology 10, 582–591.

Gu, X., Hu, J., Huang, M., 2015. K_0 of granular soils: a particulate approach. Granul. Matter 17, 703–715.

Gu, X., Huang, M., Qian, J., 2014a. DEM investigation on the evolution of microstructure in granular soils under shearing. Granul. Matter 16, 91–106.

Gu, X., Huang, M., Qian, J., 2014b. DEM investigation on the evolution of microstructure in granular soils under shearing. Granul. Matter 16, 91–106. https://doi.org/10.1007/s10035-013-0467-z

Gu, X., Li, W., Qian, J., Xu, K., 2018. Discrete element modelling of the influence of inherent anisotropy on the shear behaviour of granular soils. Eur. J. Environ. Civ. Eng. 22, s1--s18.

Guo, N., Zhao, J., 2013. The signature of shear-induced anisotropy in granular media. Comput. Geotech. 47, 1–15. https://doi.org/10.1016/j.compgeo.2012.07.002

Indraratna, B., Raut, A.K., Khabbaz, H., 2007. Constriction-based retention criterion for granular filter design. J. Geotech. Geoenvironmental Eng. 133, 266–276.

Jiang, M., Yin, Z.-Y., 2014. Influence of soil conditioning on ground deformation during longitudinal tunneling. Comptes Rendus Mécanique 342, 189–197.

Jiang, M., Yin, Z.-Y., 2012. Analysis of stress redistribution in soil and earth pressure on tunnel lining using the discrete element method. Tunn. Undergr. Sp. Technol. 32, 251–259.

Jiang, M., Yin, Z.-Y., Shen, Z., 2016. Shear band formation in lunar regolith by discrete element analyses. Granul. Matter 18, 32.

Jiang, M., Zhang, A., Shen, Z., 2020. Granular soils: from DEM simulation to constitutive modeling. Acta Geotech. 15, 1723–1744. https://doi.org/10.1007/s11440-020-00951-7

Jiang, M.J., Konrad, J.M., Leroueil, S., 2003. An efficient technique for generating homogeneous specimens for DEM studies. Comput. Geotech. 30, 579–597.

Jing, L., Kwok, C.Y., Leung, Y.F., Sobral, Y.D., 2016. Extended CFD--DEM for free-surface flow with multi-size granules. Int. J. Numer. Anal. methods Geomech. 40, 62–79.

Kafui, K.D., Thornton, C., Adams, M.J., 2002. Discrete particle-continuum fluid modelling of gas--solid fluidised beds. Chem. Eng. Sci. 57, 2395–2410.

Kawaguchi, T., Sakamoto, M., Tanaka, T., Tsuji, Y., 2000. Quasi-three-dimensional numerical simulation of spouted beds in cylinder. Powder Technol. 109, 3–12.

Kenney, T.C., Chahal, R., Chiu, E., Ofoegbu, G.I., Omange, G.N., Ume, C.A., 1985. Controlling constriction sizes of granular filters. Can. Geotech. J. 22, 32–43.

Kenney, T.C., Lau, D., 1985. Internal stability of granular filters. Can. Geotech. J. 22, 215–225.

Kloss, C., Goniva, C., Hager, A., Amberger, S., Pirker, S., 2012. Models, algorithms and validation for opensource DEM and CFD--DEM. Prog. Comput. Fluid Dyn. an Int. J. 12, 140–152.

Koch, D.L., Hill, R.J., 2001. Inertial effects in suspension and porous-media flows. Annu. Rev. Fluid Mech. 33, 619–647.

Link, J.M., Cuypers, L.A., Deen, N.G., Kuipers, J.A.M., 2005. Flow regimes in a spout--fluid bed: A combined experimental and simulation study. Chem. Eng. Sci. 60, 3425–3442.

Liu, X., Zhou, A., Shen, S. long, Li, J., Sheng, D., 2020. A micro-mechanical model for unsaturated soils based on DEM. Comput. Methods Appl. Mech. Eng. 368, 113183.

https://doi.org/10.1016/j.cma.2020.113183

Lyu, H.-M., Shen, S.-L., Yang, J., Yin, Z.-Y., 2019. Inundation analysis of metro systems with the storm water management model incorporated into a geographical information system: a case study in Shanghai. Hydrol. Earth Syst. Sci. 23, 4293–4307. https://doi.org/10.5194/hess-23-4293-2019

Midgley, T.L., Fox, G.A., Wilson, G. V, Heeren, D.M., Langendoen, E.J., Simon, A., 2012. Seepage-induced streambank erosion and instability: in situ constant-head experiments. J. Hydrol. Eng. 18, 1200–1210.

Ouyang, M., Takahashi, A., 2015. Influence of initial fines content on fabric of soils subjected to internal erosion. Can. Geotech. J. 53, 299–313.

Reboul, N., Vincens, E., Cambou, B., 2010. A computational procedure to assess the distribution of constriction sizes for an assembly of spheres. Comput. Geotech. 37, 195–206.

Richards, K.S., Reddy, K.R., 2007. Critical appraisal of piping phenomena in earth dams. Bull. Eng. Geol. Environ. 66, 381–402.

Rochim, A., Marot, D., Sibille, L., Thao Le, V., 2017. Effects of hydraulic loading history on suffusion susceptibility of cohesionless soils. J. Geotech. Geoenvironmental Eng. 143, 4017025.

Rothenburg, L., Bathurst, R., 1989. Analytical study of induced anisotropy in idealized granular material. Géotechnique 39, 601–614. https://doi.org/10.1680/geot.1990.40.4.665

Shen, S.L., Wu, H.N., Cui, Y.J., Yin, Z.Y., 2014. Long-term settlement behaviour of metro tunnels in the soft deposits of Shanghai. Tunn. Undergr. Sp. Technol. 40, 309–323. https://doi.org/10.1016/j.tust.2013.10.013

Shi, Z.-M., Zheng, H.-C., Yu, S.-B., Peng, M., Jiang, T., 2018. Application of cfd-dem to investigate seepage characteristics of landslide dam materials. Comput. Geotech. 101, 23–33.

Sibille, L., Lominé, F., Poullain, P., Sail, Y., Marot, D., 2015. Internal erosion in granular media: direct numerical simulations and energy interpretation. Hydrol. Process. 29, 2149–2163.

Sitharam, T.G., Dinesh, S. V., Shimizu, N., 2002. Micromechanical modelling of monotonic drained and undrained shear behaviour of granular media using three-dimensional DEM. Int. J. Numer. Anal. Methods Geomech. 26, 1167–1189. https://doi.org/10.1002/nag.240

Skempton, A.W., Brogan, J.M., 1994. Experiments on piping in sandy gravels. Géotechnique 44, 449–460.

Tomlinson, S.S., Vaid, Y.P., 2000. Seepage forces and confining pressure effects on piping erosion. Can. Geotech. J. 37, 1–13.

Tsuji, T., Yabumoto, K., Tanaka, T., 2008. Spontaneous structures in three-dimensional bubbling gas-fluidized bed by parallel DEM--CFD coupling simulation. Powder Technol. 184, 132–140.

Wan, C.F., Fell, R., 2004. Investigation of rate of erosion of soils in embankment dams. J. Geotech. geoenvironmental Eng. 130, 373–380.

Wang, X.-W., Yang, T.-L., Xu, Y.-S., Shen, S.-L., 2019. Evaluation of optimized depth of waterproof curtain to mitigate negative impacts during dewatering. J. Hydrol. 577, 123969. https://doi.org/https://doi.org/10.1016/j.jhydrol.2019.123969

Wang, Z.-F., Shen, S.-L., Modoni, G., 2019. Enhancing discharge of spoil to mitigate disturbance induced by horizontal jet grouting in clayey soil: Theoretical model and application. Comput. Geotech. 111, 222–228. https://doi.org/https://doi.org/10.1016/j.compgeo.2019.03.012

WEN, Y., C., 1966. Mechanics of Fluidization. Chem. Eng. Prog., Symp. Ser. 62, 100–111.

Wu, H.N., Huang, R.Q., Sun, W.J., Shen, S.L., Xu, Y.S., Liu, Y. Bin, Du, S.J., 2014. Leaking behavior of shield tunnels under the Huangpu River of Shanghai with induced hazards. Nat. Hazards 70, 1115–1132. https://doi.org/10.1007/s11069-013-0863-z

Wu, H.N., Shen, S.L., Liao, S.M., Yin, Z.Y., 2015. Longitudinal structural modelling of shield tunnels considering shearing dislocation between segmental rings. Tunn. Undergr. Sp. Technol. 50, 317–323. https://doi.org/10.1016/j.tust.2015.08.001

Xiong, H., Nicot, F., Yin, Z., 2019. From micro scale to boundary value problem: using a micromechanically based model. Acta Geotech. 14, 1307–1323. https://doi.org/10.1007/s11440-018-0717-7

Xu, Y.-S., Yan, X.-X., Shen, S.-L., Zhou, A.-N., 2019. Experimental investigation on the blocking of groundwater seepage from a waterproof curtain during pumped dewatering in an excavation. Hydrogeol. J. 27, 2659–2672. https://doi.org/10.1007/s10040-019-01992-3

Yang, J., Yin, Z.-Y., Hicher, P.-Y., Laouafa, F., 2017. A Finite Element Modeling of the Impact of Internal Erosion on the Stability of a Dike. Poromechanics VI 354–361. https://doi.org/10.1061/9780784480779.043

Yang, J., Yin, Z.-Y., Laouafa, F., Hicher, P.-Y., 2019a. Hydro-mechanical modeling of granular soils considering internal erosion. Can. Geotech. J.

Yang, J., Yin, Z.-Y., Laouafa, F., Hicher, P.-Y., 2019b. Internal erosion in dike-on-foundation modeled by a coupled hydromechanical approach. Int. J. Numer. Anal. Methods Geomech. 43, 663–683.

Yang, J., Yin, Z.-Y., Laouafa, F., Hicher, P.-Y., 2019c. Modeling coupled erosion and filtration of fine particles in granular media. Acta Geotech. 14, 1615–1627.

Yang, J., Yin, Z.-Y., Laouafa, F., Hicher, P.-Y., 2019d. Analysis of suffusion in cohesionless soils with randomly distributed porosity and fines content. Comput. Geotech. 111, 157–171.

Yin, Z.-Y., Hicher, P.-Y., Dano, C., Jin, Y.-F., 2016a. Modeling mechanical behavior of very coarse granular materials. J. Eng. Mech. 143, C4016006.

Yin, Z.-Y., Huang, H.-W., Hicher, P.-Y., 2016b. Elastoplastic modeling of sand–silt mixtures. Soils Found. 56, 520–532. https://doi.org/10.1016/j.sandf.2016.04.017

Yin, Z.-Y., Zhao, J., Hicher, P.-Y., 2014. A micromechanics-based model for sand-silt mixtures. Int. J. Solids Struct. 51, 1350–1363.

Zhang, D.-M., Gao, C.-P., Yin, Z.-Y., 2019. CFD-DEM modeling of seepage erosion around shield tunnels. Tunn. Undergr. Sp. Technol. 83, 60–72.

Zhang, D.M., Gao, C.P., Yin, Z.Y., 2019. CFD-DEM modeling of seepage erosion around shield tunnels. Tunn. Undergr. Sp. Technol. 83, 60–72. https://doi.org/10.1016/j.tust.2018.09.017

Zhang, D.M., Ma, L.X., Huang, H.W., Zhang, J., 2012. Predicting leakage-induced settlement of shield tunnels in saturated clay. Comput. Model. Eng. Sci. 89, 163–188.

Zhang, D.M., Ma, L.X., Zhang, J., Hicher, P.Y., Juang, C.H., 2015. Ground and tunnel responses induced by partial leakage in saturated clay with anisotropic permeability. Eng. Geol. 189, 104–115. https://doi.org/10.1016/j.enggeo.2015.02.005

Zhao, J., Shan, T., 2013. Coupled CFD-DEM simulation of fluid-particle interaction in geomechanics. Powder Technol. 239, 248–258.

Zhu, H.P., Zhou, Z.Y., Yang, R.Y., Yu, A.B., 2007. Discrete particle simulation of particulate systems: theoretical developments. Chem. Eng. Sci. 62, 3378–3396.